Strain pseudospins with power-law interactions: Glassy textures of a cooled coupled-map lattice

S. R. Shenoy[1] and T. Lookman[2]
[1]*School of Physics, University of Hyderabad, Hyderabad 500046, India and International Centre for Theoretical Physics, Trieste 3414, Italy*
[2]*Theoretical Division, Los Alamos National Laboratory, Los Alamos, New Mexico 87545, USA and Department of Materials Science and Engineering, University of Toronto, Toronto, Canada M5S3E*
(Received 5 May 2008; revised manuscript received 5 September 2008; published 9 October 2008)

We consider a spin-1 model of strain pseudospins $S(\vec{r})=0,\pm 1$ that arise from a triple-well Landau free energy for a square/rectangle or "austenite-martensite" structural transformation of a two-dimensional lattice. The pseudospin model has elastic-compatibility-induced *power-law anisotropic* (PLA) interactions and no quenched disorder. The iteratively solved local mean-field equations for $\langle S(\vec{r},t)\rangle$ form a temperature-dependent PLA-coupled nonlinear-map lattice, where t is the iteration "time." On cooling at a constant rate, the excess entropy shows a weak roll-off near a temperature $T=T_g$ and a sharper elbow at a lower T^*, just above a Kauzmann-type T_K where the excess entropy would have become negative. The crossover temperatures T_g, T^* decrease logarithmically with cooling rate and mark stability changes in spatiotemporal attractors of the cooled PLA-coupled map. Three phases in $\langle S(\vec{r},t)\rangle$ are found, with textures of the martensitic-variant domain walls as "inherent structures." There is a high-temperature $(T>T_g)$ fine scale phase of feathery domain walls and an intermediate temperature $(T_g>T>T^*)$ phase of mazelike domain walls, with both showing square-wave oscillations as predominantly period-two attractors but with minority-frequency subharmonic clusters. Finally, there is a low-temperature freezing $(T^*>T)$ to a static fixed point or period-one attractor of coarse, irregular bidiagonal twins, as in a strain glass. A Haar-wavelet analysis is used to identify the local attractor dynamics. A central result is that dynamically heterogeneous and mobile low-strain droplets act as catalysts, and can form correlated chains or transient "catalytic corrals" to incubate an emerging local texture. The hotspot lifetime vanishes linearly in $T-T_K$, suggesting that T_K is a dynamic spinodal limit for generating the "austenitic" catalyst, the disappearance of which drives a trapping into one of many bidiagonal glassy states. The model has relevance to martensitic or complex-oxide textures, coupled-map lattices, and configurational-glass transitions.

DOI: 10.1103/PhysRevB.78.144103 PACS number(s): 64.70.Q−, 81.30.Kf, 64.70.kj, 05.45.Ra

I. INTRODUCTION

Glass formation is a long-standing problem.[1] At finite cooling rates, crystallization is avoided and the entropy peels off from that of a liquid at a cooling-rate dependent glass transition temperature. The glassy entropy excess (over that of a crystalline solid) decreases toward zero for slow cooling rates and the slope flattens at a glass freezing temperature, thus avoiding a paradoxical negativity at an extrapolated "Kauzmann" temperature T_K,[2] where viscosities or relaxation times rise sharply.[1] Model simulations show that vibrationally masked inherent-structure configurations emerge on cooling, and dynamical heterogeneities act as mobile facilitators in their rearrangements.[3,4] Density functional theories show that there are many glassy configurational minima.[5] However, the physical meanings of the crossover temperatures and glassy structural freezing are still not fully understood.

Martensitic structural changes[1] are solid-solid transitions, with strain-tensor components as the order parameters (OPs), and have a broad transformation region and incubation delays in conversions, which are also not entirely understood. Below precursor regions, the high-symmetry "austenite" unit cells can distort in a first-order transition to form bands of twinned "martensite," separated by oriented elastic domain walls, without introducing dislocations.[6] The free energy depends on the strain tensor, which is related to the unit-cell distortion. One way to understand oriented twins is to work in the distortion-tensor, rather than the more conventional displacement-vector, representation. The no-defect condition is expressed as the St. Venant compatibility constraint linking the distortion-tensor components.[7–10] The non-OP strains are eliminated in a constrained minimization, yielding a nonlocal effective interaction between the OP strains, which has *power-law anisotropic* (PLA) decays. Simulations, in both distortion[9,10] and displacement[8] representations, show evolution into sharp twins along a preferred direction, e.g., a chosen diagonal. Recently, static and dynamic strain-glass states, distinct from known "tweed" precursors, have been experimentally detected by compositional tailoring of metallic alloys.[11]

In a configurational-glass context, anisotropic interactions with sixth-power falloff in distance have been postulated in two-dimensional (2D) spin models.[12] Glassy dynamics has also been studied in six-state dipolar models,[13] in Ising models with competing ferromagnetic/antiferromagnetic interactions,[14] and in plaquette-interaction models with special coefficients, where a Kauzmann-type temperature[2] is identified with a metastability limit.[15] Equations for the local mean field of anisotropic next-neighbor Ising (ANNI) models have been iteratively solved in space as in a nonlinear map, yielding complex phase-space trajectories and devil-staircase response to varying coupling-constant anisotropies.[16] Soft-spin models in one dimension with tilted triple minima have metastable dynamics, influenced by two possible types of kink domain-wall fronts.[17] Isotropic power-law interactions in soft-spin models, with falloff exponent

smaller than dimensionality, or other long-range models have been linked to complex metastable states, multiple spinodal branches, and non-Boltzmann entropies.[18,19] Whereas one-dimensional (1D) Potts models with power-law isotropic interactions have unusual equilibrium critical behavior,[20] Potts-type models with large-degeneracy excited states and kinetic constraints show glassy dynamics from entropy barriers or "dynamically restricted pathways for energy reduction."[21] A state-trajectory description of noninteracting Ising spins in a magnetic field, with restricted spin flips, reveals dynamical heterogeneities and glasslike freezing.[22] The above models are without random quenched disorder; if added, in nearest-neighbor couplings, glassy behavior results in Potts spin glasses and in Ising spin glasses in a magnetic field.[23,24]

A simple martensite-related discrete-spin model without quenched disorder, which shows some glasslike behavior and complex nonuniform states under cooling, would be useful in understanding martensites and glasses. For first-order transitions, the high-temperature phase remains metastable over a temperature range and could play a dynamical role.

In this paper, we consider a reduced description of a 2D square-rectangle first-order structural transformation, with the triple-minima local Landau free energy inducing three-valued strain pseudospins, $S(\vec{r})=0,\pm 1$, in a temperature-dependent effective Hamiltonian.[25] This is similar to a spin-1 Blume-Capel model[26] but with specially related temperature-dependent parameters and with added PLA interactions. The nonlinear equations for the local-average pseudospins $\sigma(\vec{r},t)\equiv\langle S(\vec{r},t)\rangle$ are solved iteratively under *constant-rate cooling*, with the iteration step "time" t having a physical interpretation. We therefore have a cooled temperature-dependent coupled-map lattice,[27] with PLA couplings. Thermodynamic functions are calculated, textures presented in coordinate and Fourier space, and dynamical heterogeneities are found, both periodic and in bursts, and analyzed using wavelet diagnostics.[28] Three phases of dynamical textures of complex domain-wall patterns, which act as "inherent structures" or local free-energy minima[3] with crossover temperatures T_g, T^* and T_K that decrease logarithmically with cooling rate,[1] are found. Three visually distinct long-lived attractors are obtained on cooling followed by holding for long times, at fixed temperatures, which are well inside three regimes. With $T \gg T_g$ there is a predominantly feathery phase of labyrinthine domain walls, with square-wave oscillations of period 2 and small clusters of periods 4, 8, …. There are local textural conversions over a range of temperatures, completed by T_g, and the system for $T_g > T > T^*$ shows a sharper maze-like phase, also with square-wave oscillations and clusters. Finally, for $T^* > T > 0$, there is a freezing to a period-one static phase of coarser and disordered twin domain walls along both diagonals. Holding at a fixed temperature just above T^*, the periodic maze attractor shows metastability and converts locally to regions of the static bidiagonal attractor. A key result is that local configurational catalysts spontaneously form to mediate the textural conversions. Low-strain "austenitic" hotspots are dynamically generated and increase to a maximum over an incubation time, forming chains enclosing cooperatively rearranging regions in "catalytic corrals" and then vanishing after the new local texture emerges. This lifetime varies linearly in $T-T_K$, so T_K acts like a dynamic spinodal temperature for hotspot catalyst disappearance.

There are many spin models without quenched disorder, showing glasslike behavior.[12–22] Our model differs in several respects and links coupled-map lattices, martensites, and glasses. It is obtained from a martensitic structural transition model, involves nonlocal PLA potentials derived from a constrained minimization of a local free energy, studies cooling-rate systematics, identifies and pictures dynamically facilitating heterogeneities, and suggests that iterative-map lattices are a natural texture-generating dynamics for nonuniform and multiple metastable states. Although experimental comparisons require further development, the general results, including configurational autocatalysis, broad transformation regions, inhomogeneous freezing, and spatiotemporal patterning, are clearly relevant to properties of martensites, configurational glasses, and strain glasses.

The plan of the paper is as follows. In Sec. II we outline the strain free energy, the derivation of the compatibility potential, and the reduction to a spin-1 model with PLA interactions. Section III presents the local mean-field equations and cooling protocol. Section IV treats the thermodynamics and crossover temperatures. Section V presents the Haar-wavelet diagnostics and pictures of the spatially and dynamically heterogeneous textures and their complex transition pathways. Finally, Sec. VI has a summary and discusses further possible work.

II. STRAIN FREE ENERGY, COMPATIBILITY CONSTRAINT, AND PSEUDOSPINS

We present (A) the 2D order-parameter strain free energy and power-law anisotropic potentials and (B) the reduction to a Hamiltonian in terms of discrete strain pseudospins.

A. Order parameter strain free energy

The distortions of the axes of a 2D square unit cell of a lattice can be described by the three components of a symmetrized distortion matrix $e_{\mu\nu}$, acting on the original Cartesian axes unit-cell vectors. Then e_{xx}, e_{yy} are stretches along the x, y directions, and $e_{xy}=e_{yx}$ are tilts of x and y unit-cell vectors toward each other. There are three physical distortions, which are the linear combinations,

$$e_1 = \frac{1}{\sqrt{2}}(e_{xx}+e_{yy}), \quad e_2 = \frac{1}{\sqrt{2}}(e_{xx}-e_{yy}), \quad e_3 = 2e_{xy}, \tag{2.1}$$

where e_1, e_2, e_3 are the compressional, deviatoric, and shear distortions, respectively, which can all be positive or negative. The scalar free energy is a function of the symmetric strain tensor $E_{\mu\nu}$, which depends on the symmetrized distortion tensor (with both linear and quadratic contributions[29,30]). We henceforth linearize the strain as simply the distortion tensor, $E_{\mu\nu} \simeq e_{\mu\nu}$.

The order parameter for the square to deform into two possible rectangular variants along x or y axis is $e_2(\vec{r})$. The variational free energy is invariant under the square-unit-cell

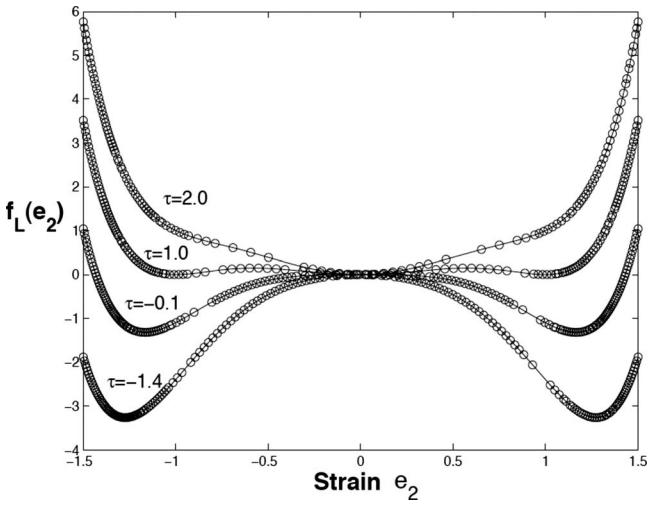

FIG. 1. Landau free-energy density of Eq. (2.3a) or $f_L(e_2)$ versus order parameter e_2 for several scaled temperatures τ.

point group and can be written in terms of the physical strains as

$$F = F_L(e_2) + F_G(\vec{\Delta}e_2) + F_{\text{non}}(e_1, e_3). \tag{2.2}$$

The sixth-power Landau term for the first-order transition is a local triple well in the OP strain, $F_L = \Sigma_{\vec{r}} f_L(e_2)$, defined on N sites $\{\vec{r}\}$ of a 2D reference lattice with fixed square unit cells, of the high-temperature austenite. Here in scaled form,[9,10]

$$\frac{f_L}{E_0} = (\tau - 1)e_2(\vec{r})^2 + e_2(\vec{r})^2(e_2(\vec{r})^2 - 1)^2 - p(\vec{r})e_2(\vec{r}), \tag{2.3a}$$

where E_0 is a unit-cell elastic energy,

$$\tau(T) \equiv (T - T_c)/(T_0 - T_c) \tag{2.3b}$$

is a scaled temperature, and $p(\vec{r})$ is an external local stress. Figure 1 shows the Landau free energy for $p(\vec{r}) = 0$. For $\tau > 4/3$ the upper spinodal temperature, there is only a single minimum at $e_2 = 0$, the austenite square-unit-cell phase. For $4/3 > \tau > 1$, there are also two symmetric metastable wells at nonzero e_2. With $\tau(T_0) = 1$ at the Landau transition temperature T_0, the triple wells become degenerate, and the nonzero martensite e_2 wells thereafter become lower in free energy. Finally, $\tau(T_c) = 0$ at the lower spinodal temperature T_c, where the metastable $e_2 = 0$ austenite well flattens and disappears. The uniform-martensite solutions for $\tau < 4/3$ are the two variants $\langle e_2 \rangle = \pm \epsilon(\tau)$, where

$$\epsilon(\tau)^2 \equiv \frac{2}{3}(1 + \sqrt{1 - 3\tau/4}), \tag{2.3c}$$

which is unity, $\epsilon(1) = 1$, at $\tau(T_0) = 1$. We henceforth scale to be dimensionless all temperatures in the physical T_0 so that $T/T_0 \to T$ and all energies in $k_B T_0$, i.e., $E_0/k_B T_0 \to E_0$.

The Ginzburg term, quadratic in nearest-neighbor differences with reference-lattice unit-cell lengths set to unity, can be written as an on site plus a nearest-neighbor ferromagnetic interaction with $\hat{\mu} = \hat{x}, \hat{y}$,

$$F_G/E_0 = \sum_{\vec{r},\hat{\mu}} \xi^2[e_2(\vec{r} + \hat{\mu}) - e_2(\vec{r})]^2$$
$$= \xi^2 \left[4 \sum_{\vec{r}} e_2(\vec{r})^2 - 2 \sum_{\langle \vec{r},\vec{r}' \rangle} e_2(\vec{r}) e_2(\vec{r}') \right]. \tag{2.3d}$$

With central difference operators, which in Fourier space are $\Delta_\mu \to iK_\mu(\vec{k}) \equiv i2 \sin(k_\mu/2)$, an equivalent form is

$$F_G/E_0 = \sum_{\vec{r}} \xi^2(\vec{\Delta}e_2)^2 = \sum_{\vec{k}} \xi^2 \vec{K}^2 |e_2(\vec{k})|^2. \tag{2.3e}$$

The non-OP term is harmonic,

$$F_{\text{non}}/E_0 = \frac{1}{2} \sum_{\vec{r}} \{A_1 e_1(\vec{r})^2 + A_3 e_3(\vec{r})^2\}$$
$$= \frac{1}{2} \sum_{\vec{k}} \{A_1 |e_1(\vec{k})|^2 + A_3 |e_3(\vec{k})|^2\}. \tag{2.3f}$$

Freely minimizing in uniform strains with wave vectors $\vec{k} = 0$, the minimum is at $e_1, e_3 = 0$ when $F_{\text{non}} = 0$. For nonuniform strains, the physical distortions are linked by St. Venant compatibility conditions.[7] These constraints ensure that lattice integrity is maintained throughout, with no defects generated, so that there is a smoothly compatible fitting together of distorted unit cells across domain walls. In two dimensions, there is a single constraint on the three distortions,[8–10] so there are two remaining free variables per unit cell, matching the 2 degrees of freedom per lattice point in the equivalent displacement representation. More generally, in d dimensions there are $d(d+1)/2$ components of the symmetrized distortion tensor and $d(d-1)/2$ constraints.

The St. Venant equations can be heuristically understood as follows. In cylindrical coordinates, an edge dislocation along the z axis has a Burgers vector in the azimuthal direction, and distortions fall off in the radial direction, i.e., there are transverse contributions. For no defects generated, the $e_{\mu\nu}$ tensor must be longitudinal.[30] Now for a longitudinal vector, the curl is zero. Thus, for a longitudinal tensor, the double curl or "incompatibility" must be zero.[7] In coordinate and Fourier space (with T denoting "transpose"),

$$\text{Inc}[\vec{e}] \equiv \vec{\Delta} \times [\vec{\Delta} \times \vec{e}(\vec{r})]^T = 0; \vec{K} \times \vec{e}(\vec{k}) \times \vec{K} = 0. \tag{2.4a}$$

In three dimensions there are three independent equations for six $e_{\mu\nu}$ components.[7,9,10] In two dimensions there is a single constraint $\Delta_x^2 e_{yy} + \Delta_y^2 e_{xx} - 2\Delta_x \Delta_y e_{xy} = 0$. In terms of physical distortions the constraint is[8–10] $\frac{1}{\sqrt{2}}(\Delta_x^2 + \Delta_y^2)e_1 - \frac{1}{\sqrt{2}}(\Delta_y^2 - \Delta_x^2)e_2 - \Delta_x \Delta_y e_3 = 0$, so an OP spatial variation $e_2(\vec{r})$ can act as a source term, inducing non-OP variations $e_1(\vec{r}), e_3(\vec{r})$, to maintain lattice integrity. In Fourier space,

$$O_1 e_1(\vec{k}) + O_2 e_2(\vec{k}) + O_3 e_3(\vec{k}) = 0, \tag{2.4b}$$

where[29] $O_1(\vec{k}) = -\frac{1}{\sqrt{2}}(K_x^2 + K_y^2)$, $O_2(\vec{k}) = \frac{1}{\sqrt{2}}(K_x^2 - K_y^2)$, $O_3(\vec{k})$

$=K_xK_y$. We need a *constrained minimization* of the free energy, which can be done analytically, since non-OP terms are harmonic. Solving for say $e_1(\vec{k})$, substituting into Eq. (2.3f), and freely minimizing in $e_3(\vec{k})$ yield the non-OP in terms of the OP strains, $e_i(\vec{k})=B_{i2}(\vec{k})e_2(\vec{k})$, with $i=1,3$, where the factors are $B_{i2}=-(O_iO_2/A_i)/\{(O_1^2/A_1)+(O_3^2/A_3)\}$. Then the compatibility-induced St. Venant interaction term between the OP strains $F_{\text{compat}}(e_2)\equiv F_{\text{non}}(e_1,e_3)$ is

$$F_{\text{compat}}/E_0=\frac{1}{2}\sum_{\vec{k}} A_1U(\vec{k})|e_2(\vec{k})|^2 \tag{2.5a}$$

or in coordinate space

$$F_{\text{compat}}/E_0=\frac{1}{2}\sum_{\vec{r},\vec{r}'} A_1U(\vec{r}-\vec{r}')e_2(\vec{r})e_2(\vec{r}'). \tag{2.5b}$$

Here the kernel $A_1U=(1-\delta_{\vec{k},0})(A_1B_{12}^2+A_3B_{32}^2)$ is

$$A_1U(\vec{k})=(1-\delta_{\vec{k},0})O_2^2/\{(O_1^2/A_1)+(O_3^2/A_3)\}, \tag{2.5c}$$

or explicitly $U(\vec{k})=(K_x^2-K_y^2)^2/\{\vec{K}^2+(2A_1/A_3)K_x^2K_y^2\}$. This is independent of $|\vec{k}|$ for long wavelengths when $\vec{K}\simeq\vec{k}$, so $U(\vec{k})\sim U(\hat{k})$, dependent only on the direction $\hat{k}$ in the Brillouin zone. [As mentioned, the uniform strain $F_{\text{non}}=0$, so we must set the kernel $U(\vec{k}=0)=0$.] For $e_2(\vec{k})$ peaking diagonally at $k_x=k_y$ or $-k_y$, the non-OP strains are expelled,[9] $e_{1,3}(\vec{k})\sim O_2(\vec{k})e_2(\vec{k})=0$, and the kernel again reaches its minimum value of zero, so diagonal domain-wall orientations are favored.

Writing Eq. (2.5b) as a pressure term in Eq. (2.3a), we see that it represents internal effective stresses at a site $\vec{r}$, which can give contradictory instructions, from different far-off strains. The PLA compatibility potential in coordinate space for $\vec{R}=\vec{r}-\vec{r}'\neq 0$, competing with Eq. (2.3e), is evaluated in simulations by a fast Fourier transform (FFT) of the kernel. An approximate form is

$$U(\vec{R})\sim\frac{\cos 4(\theta-\theta')}{\vec{R}^2}, \tag{2.6}$$

where $\hat{r}.\hat{r}'\equiv\cos(\theta-\theta')$. [Writing $U(\vec{R})$ as the 2D Fourier transform of $U(\hat{k})$ and changing variables $|\vec{k}|\to|\vec{k}|/|R|$ yield the $1/R^2$ falloff. A standard expansion of $e^{i\vec{k}\cdot\hat{R}}$ in terms of spherical Bessel functions in $|\vec{k}|$ and Legendre polynomials in $\hat{k}\cdot\hat{R}$ yields the numerator as a leading anisotropy in $\hat{R}$.] Truncating Eq. (2.6), the competing-sign[14] couplings are nearest-neighbor antiferromagnetic $(\sim+A_1/1^2)$ and next-neighbor ferromagnetic $(\sim-A_1/(\sqrt{2})^2)$. The energy E_{cell} for a square-unit-cell cut by a domain wall can be estimated. The domain wall forces some ferromagnetically coupled diagonal spins to be antiparallel, so there is a kind of "frustration" induced, which is known to imply degenerate states. The frustrated pseudospin textures trapped thermal excitations and not spin-glass-type quenched-disorder inhomogeneities. The energies are $E_{\text{cell}}\sim 2\xi^2+A_1$ for vertical or horizontal and $E_{\text{cell}}\sim 2\xi^2$ for diagonal domain walls, so again diagonal orientations are favored.

The lattice-specific fourfold anisotropy of Eq. (2.6) is from the square-unit-cell symmetry, and the falloff exponent is the dimensionality $d=2$. The "dipolar" falloff $\sim 1/R^d$ is faster than a Coulombic decay $\sim 1/R^{d-2}$ or an $\sim 1/R^\alpha$ decay[19] with $\alpha<d$. The spatial average vanishes, $\Sigma_{\vec{R}}U(\vec{R})/N=U(\vec{k}=0)=0$. The power-law exponent originates not from proximity to some critical point but from d-dimensional phase space. The property $U(\vec{k})\sim U(\hat{k})$ implies a scale-free interaction, with fluctuations of all wave vectors governed by the same strength. Plots of $U(\vec{k}), U(\vec{r})$ have been given elsewhere;[8,9] related plots are shown below.

The free energy in terms of the OP strains alone in the spirit of Landau is then

$$F(e_2)=F_L(e_2)+F_G(\vec{\Delta}e_2)+F_{\text{compat}}(e_2). \tag{2.7}$$

Below transition, the degenerate martensitic wells of F_L and the compatibility potential F_{compat} can produce oriented martensite/martensite or d_2 domain walls between bands of the competing minima, with strain changes in $\sim\pm 2\epsilon(\tau)$. (These are line solitons of the underlying ϕ^6 field theory.) The presence of zero-strain minima suggests a second martensite/austenite or d_1 domain wall, with smaller changes in $\sim\pm\epsilon(\tau)$. Bechhoefer *et al.*[17] considered a tilted triple-well 1D soft-spin model, finding that there are two types of kink domain walls similar to d_2, d_1, with different velocities, which dynamically produce dominant regions of a long-lived metastable phase. In our 2D model, we will find later that a short-lived local domain-wall splitting/rejoining $(d_2\to 2d_1\to d_2)$ plays a catalytic role in incubating patterns of d_2 martensitic domain walls.

B. Pseudospin Hamiltonian

The local Boltzmann factor $e^{-\beta f_L}$ has three peaks in the OP strain at free-energy minima $\langle e_2(\vec{r})\rangle\equiv\langle|e_2(\vec{r})|S(\vec{r})\rangle=0,\pm\epsilon(\tau)$, where $S(\vec{r})=0,\pm 1$ represents the austenite (0) and martensite-variant (± 1) choices made in the displacive transition. We make the approximation, which is meaningful only in the strain representation,

$$e_2(\vec{r})\to\epsilon(\tau)S(\vec{r}), \tag{2.8a}$$

where the pseudospin $S(\vec{r})$ has values

$$S(\vec{r})=0,\pm 1, \tag{2.8b}$$

and $\epsilon(\tau)$ is as in Eq. (2.3c), for $4/3>\tau(T)>\tau(T=0)$. We allow the intrinsic possibility of all three types of unit cells or three spin values at all temperatures, since internal stresses from neighboring variations could tilt the Landau free energy to locally cause their appearance.

With the substitution of Eqs. (2.8a) and (2.8b) and the relations $S(\vec{r})^6=S(\vec{r})^4=S(\vec{r})^2=0$ or 1, the nonlinear OP-strain free energy of Eq. (2.7) collapses to a pseudospin "Hamiltonian" suggested earlier[25] with

$$H(T)\equiv F[e_2(\vec{r})\to\epsilon(\tau)S(\vec{r})]. \tag{2.9}$$

An analogy has been made between austenite/martensite strains and discrete pseudospin values in models with general coupling constants.[31] Our Hamiltonian (2.9) differs, as

the pseudospin values arise from OP choices within a variational free energy, yielding specific coupling constants whose T-dependent sign changes carry the displacive first-order transition, as below.

The temperature-dependent model Hamiltonian, bilinear in the pseudospins, with single-site, nearest-neighbor, and PLA interaction terms is

$$\beta H = \frac{D_0}{2}\left\{ \sum_{\vec{r}} g_0 S(\vec{r})^2 + \xi^2[\vec{\Delta} S(\vec{r})]^2 + \frac{A_1}{2}\sum_{\vec{r},\vec{r}'} U(\vec{r}-\vec{r}')S(\vec{r})S(\vec{r}') - \sum_{\vec{r}} p(\vec{r})S(\vec{r})/\epsilon \right\}, \quad (2.10a)$$

with

$$f_L(\epsilon) = E_0 g_0(\tau)\epsilon(\tau)^2,$$

$$g_0(\tau) \equiv (\tau - 1) + (\epsilon^2 - 1)^2, \quad (2.10b)$$

and with a scaled $\beta = 1/T$, we have $D_0 \equiv 2(E_0/T)\epsilon(\tau)^2$. In a strictly uniform mean-field approximation the average $\langle \beta H \rangle \simeq \langle \beta H_{\mathrm{MF}} \rangle = N\beta f_L \langle S \rangle^2$ and the $\langle S \rangle = 0$ austenite state is preferred for $T \geq T_0$ or $\tau \geq 1$ when $f_L > 0$, while $\langle S \rangle = \pm 1$ is preferred for $T < T_0$ or $\tau < 1$ below transition when $f_L < 0$. Thus, for the uniform case, the magnitude jump and sign locking of the OP, both occur at the same transition temperature; the pseudospin description faithfully reproduces the first-order Landau transition of Eq. (2.3a).

The model [Eq. (2.10a) with Eq. (2.3d)] is related to a temperature-dependent version of the "classical spin-1" or Blume-Capel model[26] $\beta H = -\beta J \Sigma_{\langle r,r' \rangle} S_r S_{r'} + \beta J' \Sigma_r S_r^2$, but with special parameter relations $\{\beta J(T) = D_0(T)\xi^2, \beta J'(T) = \frac{1}{2} D_0(T)[g_0(\tau) + 4\xi^2]\}$, and now including PLA $\sim 1/R^d$ interactions, with $\vec{R}$-direction-specific anisotropies. The model also differs from dipolar models with $\sim 1/R^d$ interactions, as these have dipole-orientation-specific anisotropies.[13] The model is actually one of a larger class of "clock-zero" models, with pseudospins obtained from scaled Landau free energies with N_V variants described by N_{OP} strain order parameters.[30] The pseudospins have N_V clock values on a unit sphere plus a zero state at the center, so there are $(N_V + 1)$ values. For the 2D square/rectangle transition $N_V = 2, N_{\mathrm{OP}} = 1$, and in this case the $(2+1)$ clock-zero states happen to be equivalent to a three-state spin-1 model. However, the 2D triangle/face-centered-rectangle transition and the 3D cubic/tetragonal transition, both have $N_{\mathrm{OP}} = 2$ component order parameters (e_2, e_3), with $N_V = 3$ Landau minima.[9] Their pseudospin Hamiltonian corresponds to a $(3+1)$-state clock-zero model (plus different 2D/3D PLA couplings), which in this case is not equivalent to a four-state spin-3/2 model. These and other clock-zero models will be studied elsewhere.

With Fourier expansions,

$$S(\vec{r}) = \frac{1}{\sqrt{N}}\sum_{\vec{k}} S(\vec{k}) e^{i\vec{k}\cdot\vec{r}}; U(\vec{R}) = \frac{1}{N}\sum_{\vec{k}} U(\vec{k}) e^{i\vec{k}\cdot\vec{R}},$$

the Hamiltonian is diagonal in Fourier space,

$$\beta H = \frac{1}{2}\sum_{\vec{k}} Q_0(\vec{k})|S(\vec{k})|^2, \quad (2.11a)$$

where $S(\vec{k})^* = S(-\vec{k})$ and

$$Q_0(\vec{k}) \equiv D_0\left\{ g_0(\tau) + \xi^2 \vec{K}^2 + \frac{1}{2} A_1 U(\vec{k}) \right\}. \quad (2.11b)$$

Monte Carlo quench simulations[32] of Hamiltonian (2.10a) or (2.11a) eventually yield sharp domain walls oriented along a diagonal, as in simulations of the full continuous-variable strain model.[9,10] However, to study long-lived transients and glassy behavior, we pursue a *local mean-field* approximation under a *cooling ramp*. If the temperature is swept faster than the uniform-martensite state that can be established, fine scale textures in $S(\vec{k})$ will be spread over much of the Brillouin zone. The potential that they see can be separated into an averaged temperature shift and a shifted potential that averages to zero over the Brillouin zone. The shifted potential is

$$V(\vec{k}) = \xi^2\{\vec{K}^2 - [\vec{K}^2]\} + \frac{1}{2}\{A_1 U(\vec{k}) - [A_1 U(\vec{k})]\}, \quad (2.12)$$

where square brackets denote Brillouin-zone averages, evaluated as $[U(\vec{k})] = \Sigma_{\vec{k}} U(\vec{k})/N = 0.29$ and $[\vec{K}^2] = 4$. The compatibility potential $U(\vec{R})$ and shifted potential $V(\vec{k})$ are shown as relief plots in Fig. 2. Note the sign changes and power-law profiles of $U(\vec{R})$. The $V(\vec{k})$ wave-vector channels are shifted by the temperature τ in Q_0 and dynamically restrict the pathways for free-energy reduction.

Free energy barriers are combinations of energy and entropy barriers. (A pure energy barrier for a golf ball is a ridge followed by a broad funnel-shaped surface leading to a hole: if the ball has energy to surmount the ridge at any forward angle, it drops into the hole. A pure entropy barrier[21] is a flat surface, with many forward trajectories missing the hole, and only a geometrically restricted fraction of phase-space trajectories dropping in.) Ritort and Mansfield[21] considered entropy barriers in kinetically biased models with many degenerate excited states, and only a configurationally restricted fraction of spins allowed to drop toward the ground state. We note that configurational transitions from one free-energy valley to the next are along paths crossing saddle-point mountain passes of barrier height $\Delta_b F$. The transition weight is $\sim e^{-\beta\Delta_b F} = e^{-\beta\{\Delta_b U - T\Delta_b S\}} \sim \Omega e^{-\beta\Delta_b U}$, where the entropy difference between the transition-pathway and valley configurations is $\Delta_b S \sim \ln \Omega$. If the relative number of transitional pathways Ω becomes small, then an "ergodicity-breaking" transition can occur. Metastable configurations can then be preserved for long times by large entropy barriers $|\Delta_b S|$ or the sparseness of pathways, even if energy barriers $\Delta_b U$ along that path are small or even zero.

The domain-wall configurations can be described by directed-segment variables $\vec{j}(\vec{r}) = \hat{z} \times \vec{\Delta} S(\vec{r})$ along the walls or in Fourier space by $j_x(\vec{k}) = -iK_y S(\vec{k}), j_y(\vec{k}) = +iK_x S(\vec{k})$. The Hamiltonian of Eqs. (2.11a) and (2.11b) can be formally written in terms of an anisotropic Coulomb-type potential between these "current-density" segments,

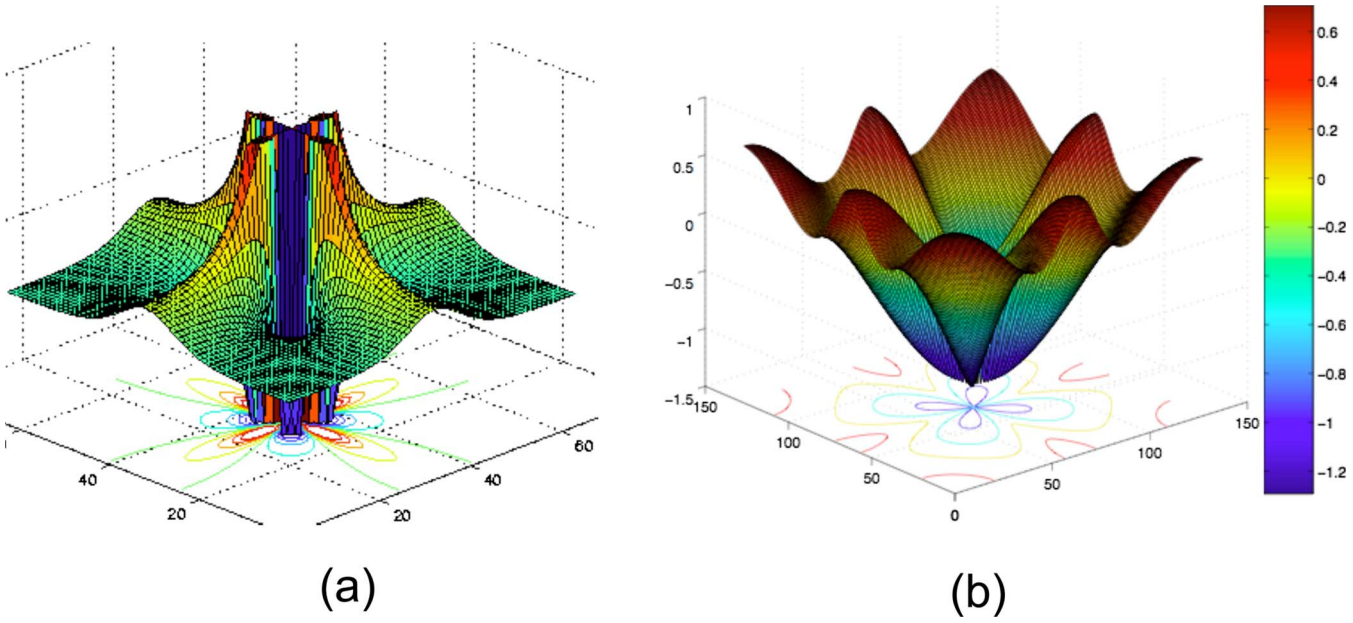

FIG. 2. (Color online) Relief plots of the compatibility potential: (a) coordinate space potential of Eqs. (2.5a), (2.5b), and (2.5c) or $U(\vec{r})$ versus (x,y); (b) Fourier-space shifted potential of Eq. (2.12) or $V(\vec{k})$ versus (k_x,k_y).

$$\beta H = \frac{1}{2}\sum_{\vec{k}\neq 0}\frac{Q_0(\vec{k})}{\vec{K}^2}|\vec{j}(\vec{k})|^2 + \frac{1}{2}D_0 g_0 S(\vec{k}=0)^2, \quad (2.13)$$

which manifestly obey a conservation law, $\vec{\Delta}\cdot\vec{j}(\vec{r})=0$. Thus, domain walls either form closed loops or end on boundaries.

As noted earlier,[10] these N_{domain} extended objects of reduced dimensionality, stretching across the $N=L^d$ lattice, have excited-state cost of $\sim N_{\text{domain}}\xi L^{d-1}$, above the uniform ground-state energy $\sim L^d$. Such textures can be "quasidegenerate" with the global minimum, i.e., have an energy-density difference of $\sim \xi N_{\text{domain}}/L \sim 1/L$. Since domain walls can be placed anywhere, there are exponentially many such patterns, which are inherent structures, or local basins of attraction in configuration space,[3] with large free-energy barriers for removal. Thus, domain-wall textural minima can be numerous, locally stable, and long lived.

III. LOCAL MEAN-FIELD EQUATIONS AND COUPLED-MAP LATTICE

Here we present a coupled-map lattice[27] and cooling protocol. We consider a *local* mean field, which in Fourier or coordinate space is

$$\sigma(\vec{k}) \equiv \langle S(\vec{k})\rangle; \sigma(\vec{r}) \equiv \langle S(\vec{r})\rangle, \quad (3.1a)$$

where angular brackets are statistical averages. We do a mean-field approximation such that (i) all Hamiltonian terms are substituted/approximated in the same way and (ii) the mean-field Hamiltonian is linear in $S(\vec{r})$ plus a constant and vanishes for zero mean field. Three implementations all yield the same result.

In Fourier space for Eqs. (2.11a) and (2.11b), the substitution is

$$|S(\vec{k})|^2 \to S(\vec{k})\sigma(\vec{k})^* + \sigma(\vec{k})S(\vec{k})^* - |\sigma(\vec{k})|^2. \quad (3.1b)$$

In coordinate space for Eqs. (2.10a) and (2.10b), $\beta H = \frac{1}{2}\Sigma_{\vec{r}} S(\vec{r})h_S(\vec{r})$, where

$$h_S(\vec{r}) \equiv D_0\left\{ g_0 S(\vec{r}) - \xi^2\vec{\Delta}^2 S(\vec{r}) + \frac{A_1}{2}\sum_{\vec{r}'} U(\vec{r}-\vec{r}')S(\vec{r}')\right\},$$

and the local mean-field substitution is

$$S(\vec{r})h_S(\vec{r}) \to \sigma(\vec{r})h_S(\vec{r}) + S(\vec{r})h_\sigma(\vec{r}) - \sigma(\vec{r})h_\sigma(\vec{r}). \quad (3.1c)$$

Finally, one could obtain mean-field equations by minimizing $\Phi = \langle \beta H\rangle + T\rho \ln \rho$ with respect to the variational Boltzmann weight[33] $\rho = \Pi_{\vec{k}}\rho(\vec{k})$, diagonal in $\vec{k}$ like the exact Hamiltonian, and with $\langle S(\vec{k})\rangle$ and $\langle S(-\vec{k})\rangle$ treated as independent. The mean-field Hamiltonians in Fourier and coordinate space, with external $p=0$, are

$$\beta H_{\text{MF}} = \sum_{\vec{k}} Q(\vec{k})^* S(\vec{k}) - \frac{1}{2}\sum_{\vec{k}} Q(\vec{k})^*\sigma(\vec{k}), \quad (3.2a)$$

$$\beta H_{\text{MF}} = \sum_{\vec{r}} Q(\vec{r})S(\vec{r}) - \frac{1}{2}\sum_{\vec{r}} Q(\vec{r})\sigma(\vec{r}). \quad (3.2b)$$

Here $Q(\vec{k}) = h_\sigma(\vec{k})$ in Fourier and $Q(\vec{r}) = h_\sigma(\vec{r})$ in coordinate space are defined as

$$Q(\vec{k}) \equiv Q_0(\vec{k})\sigma(\vec{k}), \quad (3.2c)$$

$$\frac{Q(\vec{r})}{D_0} \equiv \left\{ g_0\sigma(\vec{r}) - \xi^2\vec{\Delta}^2\sigma(\vec{r}) + \frac{A_1}{2}\sum_{\vec{r}'} U(\vec{r}-\vec{r}')\sigma(\vec{r}') \right\}. \tag{3.2d}$$

From Eqs. (2.10a) and (3.2b), $Q(\vec{r})$ is a mean-field internal stress. Then the self-consistency equations for $\{\sigma(\vec{r})\}$ are

$$\sigma(\vec{r}) = \sum_{S=0,\pm 1} S(\vec{r})e^{-\beta H_{\mathrm{MF}}} \Big/ Z_{\mathrm{MF}} = M(\{\sigma\}), \tag{3.3a}$$

where $Z_{\mathrm{MF}}=\Sigma_S e^{-\beta H_{\mathrm{MF}}}$, and the map M is

$$M(\{\sigma\}) \equiv -2\sinh Q(\vec{r})/\{1+2\cosh Q(\vec{r})\}. \tag{3.3b}$$

These can be solved iteratively, with the iteration-step label as a discrete time, whose physical interpretation is discussed below. We thus have a PLA-coupled nonlinear-map lattice, with temperature-dependent control parameters,

$$\sigma(\vec{r},t+1) = M(\{\sigma(\vec{r}',t)\}). \tag{3.4}$$

In general, nonlinear maps can have chaotic, periodic, or fixed-point attractors. Coupled-map lattices with Laplacian nearest-neighbor couplings and global couplings, feeding into each site the average of all outputs can support synchronized clusters of periodic attractors.[27,34] Sinha considered[35] a random (and hence *far-neighbor*) rewiring of a 1D coupled logistic-map lattice. She found that the effective long-range couplings stabilize the (otherwise unstable) fixed-point attractor or period-one "synchronous" state. Garrahan and Chandler considered[22] noninteracting Ising spins, with spatial correlations induced through nearest-neighbor restrictions on allowed spin flips, and found a dynamical arrest of state-vector trajectories on cooling. In our case, with a similar N-component state vector $\vec{R}_{\vec{r}}(t) \equiv \{\sigma(\vec{r},t)\}$, the map $M[\vec{R}_{\vec{r}}(t)]$ determines the evolution along the trajectory to $\vec{R}_{\vec{r}}(t+1)$, and an "entropy crisis in trajectory space"[22] is simply the onset of a fixed-point attractor.

It is convenient to separate out $\sigma(\vec{r},t)=\sigma_0(t)+\tilde{\sigma}(\vec{r},t)$, with a uniform mean-field part $\sigma_0(t)$ and a spatially varying $\vec{k} \neq 0$ part $\tilde{\sigma}(\vec{r},t)$, to yield linked maps (where again square brackets are lattice averages),

$$\sigma_0(t+1) = \frac{1}{N}\sum_{\vec{r}} M(\{\sigma(\vec{r}',t)\}) \equiv [M], \tag{3.5a}$$

$$\tilde{\sigma}(\vec{r},t+1) = M(\{\sigma(\vec{r}',t)\}) - [M]. \tag{3.5b}$$

Monte Carlo and other simulations usually follow a "quench-and-hold" approach, with random initial spins, corresponding to a high temperature, then evolved at $T=T_{\mathrm{final}}$, i.e., suddenly cooled at an "infinite" rate, followed by waiting for an infinite time t_h, to reach a unique global-minimum equilibrium state. However, to investigate multiple metastable minima with long lifetimes in glassy systems, it is useful to study the response to a more gradual and controlled cooling protocol. We start from an initial high temperature T_{initial} with a flat stochastic distribution in a range ± 1 and a random seed σ_{random}, yielding a set of initial mean-field spins $\{\sigma(\vec{r},t=0)\}$. As iteration proceeds, the temperature is reduced at a constant cooling rate $|\dot{T}|$ to a final fixed temperature T_{final}, where the system is "*annealed*" or held at this temperature, for a further holding time interval t_h. The five preparation parameters $\{\sigma_{\mathrm{random}}, T_{\mathrm{initial}}, T_{\mathrm{final}}, |\dot{T}|, 1/t_h\}$ characterize the thermal history of the metastable state accessed. (Equilibrium thermodynamics implicitly considers the limit $|\dot{T}| \to 0$ and $1/t_h \to 0$, with states then independent of thermal history.) The cooling ramp is

$$T(t) = T_{\mathrm{initial}} - |\dot{T}|t \quad (t_{\mathrm{final}} > t > 0), \tag{3.6a}$$

$$= T_{\mathrm{final}} \quad (t_h + t_{\mathrm{final}} > t \geq t_{\mathrm{final}}).$$

The unit time-step cooling corresponds, in a continuous-time sweep, to a sequence of identical microquenches of depth $\Delta T=-|\dot{T}|$. In terms of the scaled temperature, the cooling ramp is

$$\tau\{T(t)\} = \tau_{\mathrm{initial}} - \frac{|\dot{T}|}{(T_0 - T_c)}t \quad (t_{\mathrm{final}} > t > 0) = \tau_{\mathrm{final}} \quad (t_h + t_{\mathrm{final}} > t \geq t_{\mathrm{final}}), \tag{3.6b}$$

where $\tau_{\mathrm{initial}}=\tau(T_{\mathrm{initial}})$, $\tau_{\mathrm{final}}=\tau(T_{\mathrm{final}})$, and $t_{\mathrm{final}}=(\tau_{\mathrm{initial}} - \tau_{\mathrm{final}})(T_0-T_c)/|\dot{T}|$.

A heuristic argument suggests that the discrete-time step of Eq. (3.4) may have a physical meaning. On cooling a system at a finite rate, there will be spatial fluctuations in the order parameter as excess entropy is swept along. Suppose the local entropy and energy $s\{\sigma(\vec{r},t)\}, u\{\sigma(\vec{r},t)\}$ define a temperature $T=\{\partial s(\sigma)/\partial u(\sigma)\}^{-1}$. Here T must be the same throughout the system, so the canonical-ensemble and mean-field equations derived from it are applicable to find the textures of nonuniform strain at uniform temperature. Then on further cooling by $|\Delta T|$ at a rate $|\dot{T}|$, there is a minimum time scale t_{min} for heat to flow to the external heat bath and for local energy/entropy relaxation through strain changes $\delta\sigma(\vec{r},t)$. A new uniform temperature $T-|\Delta T|=\{\partial s(\sigma+\delta\sigma)/\partial u(\sigma+\delta\sigma)\}^{-1}$ is established, where $\Delta T=-|\dot{T}|t_{\mathrm{min}}$: the canonical-ensemble mean-field equations are stroboscopically valid. Setting $t_{\mathrm{min}}=1$, one therefore has a *discrete-time* map. This is analogous to a larger-dimensionality dynamical system having the order-parameter space as a "Poincare slice," to which the trajectory returns, but only after a delay. Thus, a coupled nonlinear-map lattice can serve as a natural description for the slow relaxation of nonuniformly strained systems.

IV. THERMODYNAMICS AND TEXTURE DIAGNOSTICS

In this section we evaluate and plot thermodynamic functions per unit cell versus temperature. The partition function is

$$Z = \sum_{\{S\}} e^{-\beta H(T)}, \tag{4.1a}$$

with $H(T)$ as the full Hamiltonian of Eqs. (2.10a) or (2.11a). The free energy per unit cell is $f=F/N=-(1/\beta N)\ln Z$. The

entropy per unit cell $s=S/N=-\frac{1}{N}\partial F/\partial T$ yields

$$s=(u-f)/T, \tag{4.1b}$$

where the internal energy per cell $u=U/N$ is

$$\beta u=\frac{\beta}{N}\{\langle H(T)\rangle - T\langle \partial H(T)/\partial T\rangle\}, \tag{4.1c}$$

and the second term comes from the temperature dependence of the Hamiltonian in Eq. (4.1a). It is convenient to write Eqs. (2.11a) and (2.11b) as

$$\frac{H(T)}{N}=E_0\left\{J_0(S)\frac{f_L(\epsilon)}{E_0}+J_1(S)\epsilon(\tau)^2\right\}, \tag{4.2a}$$

where

$$J_0(S)\equiv\frac{1}{N}\sum_{\vec{k}}|S(\vec{k})|^2, \tag{4.2b}$$

$$J_1(S)\equiv\frac{1}{N}\sum_{\vec{k}\neq 0}\left\{\xi^2\vec{K}^2+\frac{1}{2}A_1U(\vec{k})\right\}|S(\vec{k})|^2. \tag{4.2c}$$

Doing T derivatives of Eq. (4.1c), with τ as in Eq. (2.3c), and then taking mean fields,

$$\beta u=\frac{\langle\beta H\rangle}{N}-\frac{E_0T\beta}{(T_0-T_c)}\left\{\frac{J_0(\sigma)}{E_0}\frac{\partial f_L}{\partial\tau}+J_1(\sigma)\frac{\partial\epsilon^2}{\partial\tau}\right\}, \tag{4.3a}$$

where

$$\frac{\langle\beta H\rangle}{N}=\beta E_0\left\{J_0(\sigma)\frac{f_L(\epsilon)}{E_0}+J_1(\sigma)\epsilon^2\right\}. \tag{4.3b}$$

The mean-field entropy is from Eq. (4.1b), where the mean-field free energy using $\beta H_{\rm MF}$ of Eqs. (3.2a), (3.2b), (3.2c), and (3.2d) in Eq. (4.1a) is

$$\beta f=-\frac{1}{N}\sum_r \ln\frac{1}{3}\{1+2\cosh Q(\vec{r})\}-\frac{1}{2N}\sum_{\vec{k}}Q_0(\vec{k})|\sigma(\vec{k})|^2. \tag{4.3c}$$

In the limit of suppressing nonuniform mean-field contributions $J_1(\sigma)\to 0, J_0(\sigma)\to\sigma_0^2=1$ and for $f_L(\epsilon)<0$ and $e^{-D_0f_L}\gg 1$, the energy (4.3a) and free energy (4.3c) become Landau expressions (with $\partial f_L/\partial\epsilon=0$),

$$u_L(\epsilon)=f_L(\epsilon)+Ts_L(\epsilon), \tag{4.4a}$$

$$f_L(\epsilon)/E_0=(\tau-1)\epsilon^2+\epsilon^2(\epsilon^2-1)^2, \tag{4.4b}$$

$$s_L(\epsilon)=-\partial f_L/\partial T=-\frac{E_0}{T_0-T_c}\epsilon^2. \tag{4.4c}$$

Simulations are done for a 128×128 lattice and periodic boundary conditions. We take $\xi=1/2$, $A_1=4$, $A_3/A_1=1/2$, $E_0=3$, $T_0=1$, $T_c=0.9$, $\tau_{\rm initial}=4/3$ and apply various cooling rates $0.1>|\dot{T}|>0.0001$, with holding times up to $t_h=2^M, M=10$. Initially, we cool to all the way to zero temperature $T_{\rm final}=0$ or $\tau_{\rm final}=\tau(0)=-T_c/(T_0-T_c)=-9$ and later take nonzero final annealing temperatures. It is convenient to do a FFT on the inputs $\{\sigma(\vec{r},t)\}$ to evaluate $Q(\vec{k})$ of Eq. (3.2c) and a reverse FFT to get $Q(\vec{r})$ used in the map [Eqs. (3.3b)], yielding the outputs $\{\sigma(\vec{r},t+1)\}$. In practice, we find that the nonuniform $\tilde{\sigma}\sim O(1)$ dominates, with negligible uniform contribution $\sigma_0\sim O(10^{-3}-10^{-5})$.

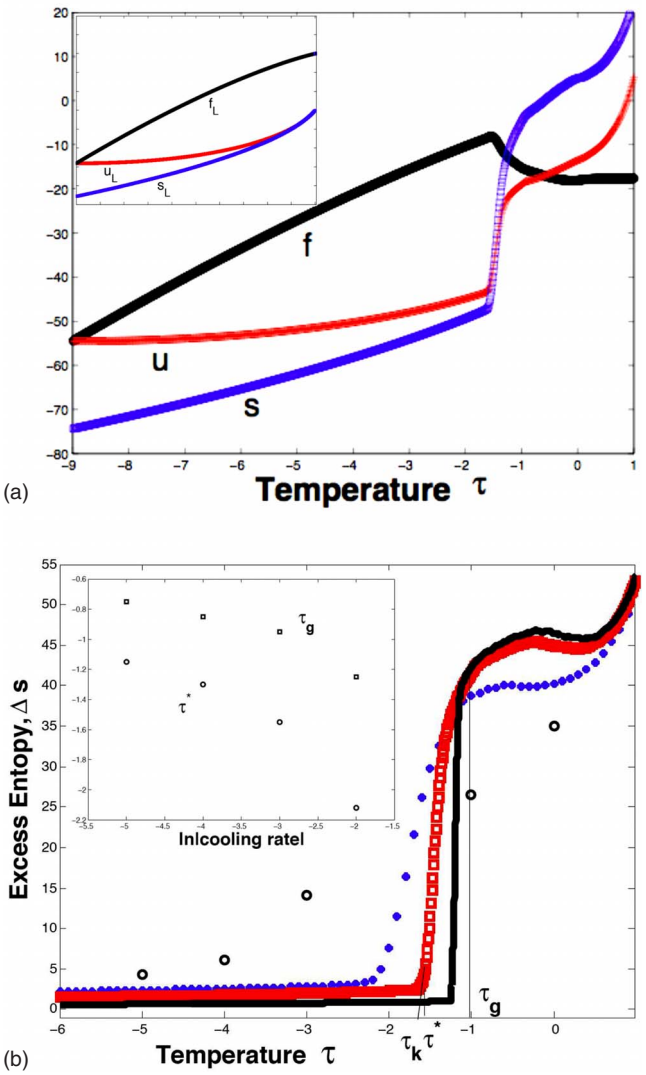

FIG. 3. (Color online) Thermodynamic potentials per unit cell for nonuniform textures versus scaled temperature $\tau(T)$ for cooling down to zero temperature at various rates: (a) for cooling rate $|\dot{T}|=0.001$, the free energy f, internal energy u, and entropy s of Eqs. (4.3a), (4.3b), and (4.3c). [Inset: the corresponding $f_L(\epsilon), u_L(\epsilon), s_L(\epsilon)$ versus τ of Eqs. (4.4a), (4.4b), and (4.4c) for a uniform mean-field order parameter $\epsilon(\tau)$.] (b) The excess entropy $\Delta s\equiv s-s_L(\epsilon)$ is shown for four cooling rates $|\dot{T}|=0.0001, 0.001, 0.01, 0.1$, where the rates increase from right to left for the curves at low temperatures. For $|\dot{T}|=0.001$ the crossover temperatures τ_g, τ^*, τ_K are indicated. [Inset: crossover temperatures τ_g and τ^* versus $\log(|\dot{T}|)$.]

Figure 3 shows the thermodynamic functions. The inset of Fig. 3(a) with horizontal axis τ between $\tau(0)=-9$ and $+1$ shows the uniform-state thermodynamics of Eqs. (4.4a), (4.4b), and (4.4c), with an entropy/energy jump at the $\tau=1$

first-order transition and a continuous free energy. The main Fig. 3(a) shows the thermodynamic potentials per cell f,s,u for cooling to $T_{\text{final}}=0$ at $|\dot{T}|=0.001$. The entropy and energy swept along on cooling from $\tau=4/3$, both show initial buildups, and the larger entropy buildup induces an initial bump in the free energy $f=u-Ts$. Figure 3(b) shows the excess entropy over the Landau value, $\Delta s \equiv s-s_L(\epsilon)$ versus τ, for various cooling rates, 0.0001, 0.001, 0.01, and 0.1. The excess-entropy curves show cooling-rate dependent roll-offs, followed by almost linear decreases, and then elbowlike changes to lines of much lower slope, as will be understood later. Temperatures $\tau_g=\tau(T_g)$ and $\tau^*=\tau(T^*)$ from textural diagnostics below are marked for the $|\dot{T}|=0.001$ curve. Extrapolating the high-slope portion to intersect the temperature axis marks a Kauzmann-type temperature[1,2] τ_K.

It is useful to define two Fourier diagnostics related to the domain-wall orientations (see later) through

$$G_2=\sum_{\vec{k}} P(\vec{k})(O_2/O_1)^2, \quad G_3=\sum_{\vec{k}} P(\vec{k})(O_3/O_1)^2, \quad (4.5)$$

where $P(\vec{k})=|\sigma(\vec{k})|^2/\Sigma_{\vec{k}}|\sigma(\vec{k})|^2$. A peak in G_2 and a coincident dip in G_3 versus τ define a temperature τ_g and coincident onsets of flattening in both define a τ^*. These correspond to the structures in the excess entropy mentioned above. The inset of Fig. 3(b) shows that the crossover temperatures τ_g,τ^* decrease logarithmically with cooling rate as can be understood. Domain-wall segments of multiscale textures will face a range of local energy barriers. For cooling faster than some of these relaxation rates, the higher-barrier $>E_{\text{equ}}$ structures will not equilibrate fully, where $|\dot{T}|\geq e^{-\beta E_{\text{equ}}}$. The textural crossover temperatures T_g,T^* will naturally depend on E_{equ} and hence on $\sim\ln|\dot{T}|$.

V. TEXTURES AND TRANSITION PATHWAYS

We only touch upon the surprisingly rich attractors of the PLA-coupled nonlinear-map lattice in this section that presents (A) spatiotemporal textures in a wavelet analysis and (B) dynamical transition pathways.

A. Textures and Haar-wavelet spectra

For 1D globally coupled logistic maps, the evolution of lattice variables shows up in space-time plots as fernlike patterns.[27] On cooling at $|\dot{T}|=0.001$ to zero temperature, we do a Kaneko-type space-time plot by taking an $x=0$ or 1D slice of the 2D space. In Fig. 4(a), colors depict $\sigma(x=0,y,t)$ versus y and t, and three evolving phases can be seen. The crossover temperatures are $\tau_g=-0.95$ and $\tau^*=-1.57$, corresponding to the $\tau(t)$ cooled through. From the color bar, the σ values are $\sim\pm 1$, so the map essentially evolves the domain walls rather than the strain magnitudes. The three phases are clearly seen in 2D color snapshots of $\sigma(\vec{r},t)$ taken at three temperatures while cooling to zero (not shown).

Figure 4(b) shows that the same three textures arise for $|\dot{T}|=0.001$ if we cool and hold to three nonzero final temperatures $\tau=\tau_{\text{final}}$ well within the three regimes below, with

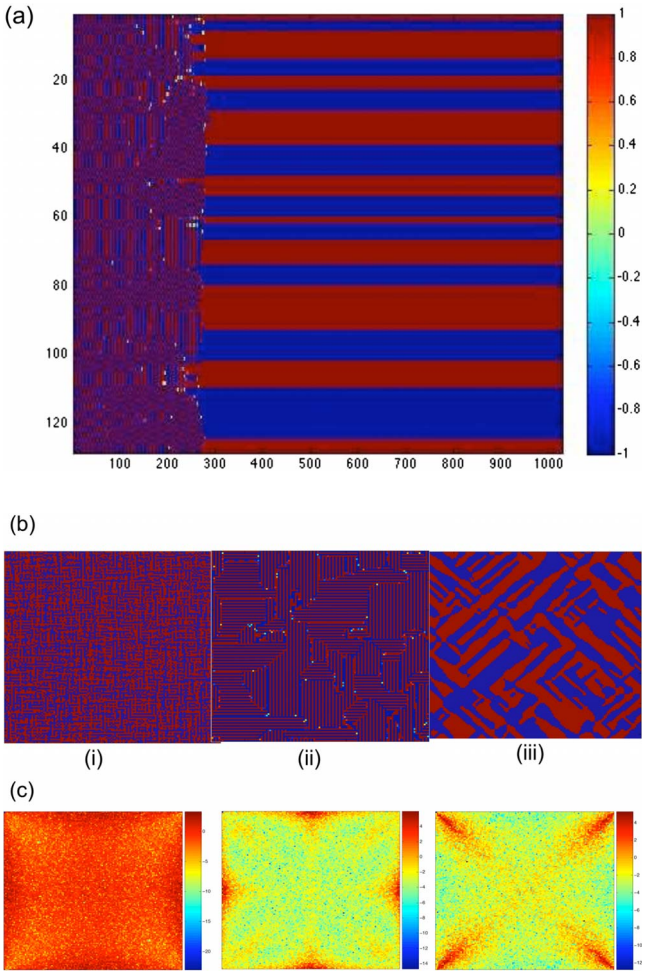

FIG. 4. (Color online) Three types of textures all on cooling at a rate $|\dot{T}|=0.001$: (a) space-time evolution color plots on cooling-to-zero temperature, showing OP strains $\sigma(x=0,y,t)$ versus (y,t). (b) Coordinate-space color plots of $\sigma(\vec{r},t)$ versus (x,y) on cooling to three final scaled temperatures $\tau(T)$ and holding for long times, showing (i) feathery ($\tau=+0.6$), (ii) maze ($\tau=-1.0$), and (iii) bidiagonal ($\tau=-2.5$) phases. The holding temperatures are well within the three temperature ranges of $4/3>\tau>(\tau_g=-0.95)$, $\tau_g>\tau>(\tau^*=-1.57)$, and $\tau^*>(\tau_K=-1.61)>\tau>[\tau(T=0)=-9]$. (c) Fourier-space color plots of $\ln|\sigma(\vec{k})|^2$ versus (k_x,k_y) for the three phases of (b) above.

phases remaining stable over holding times $t_h\sim 10^4$ [compare y axis slices of Fig. 4(b) with those of Fig. 4(a)]. Figure 4(b) shows that (i) for $4/3>(\tau=+0.6)>\tau_g$ there is a predominantly feathery phase of short domain walls, with many stubby sidebars and loops. As the holding temperature is lowered in different cool-and-hold runs, this locally converts over a broad range of temperatures to patches of the maze phase, and (ii) for $\tau_g>(\tau=-1.0)>\tau^*$, there is entirely a maze phase of long narrow domains along horizontal or vertical axes forming striped grains with irregular boundaries. Finally, (iii) for $\tau^*>(\tau=-2.5)>\tau(0)$ there is a "bidiagonal" phase with coarse domains and wandering walls along both diagonals. This thermal-disorder texture is like the irregular states passed through in more conventional dynamics,[8–10] en route to the final state of sharp twins along single diagonals,

so it has a strain-glass-like character.[11] The three textures are anisotropic and *multiscale* in coordinate space. This is also seen in Fourier-space plots of Fig. 4(c), which shows for the same three temperatures, logarithmic color plots of $\ln|\sigma(\vec{k})|^2$ versus (k_x,k_y) spread across the Brillouin zone. The differing anisotropies motivate the diagnostics of Eq. (4.5).

The PLA interactions affect textures at all temperatures. Switching them off by setting $A_1=0$ yields checkerboard textures at high temperatures and shapeless blobs at low temperatures. The zero-elastic constant model is however unphysical as it is infinitely compressible and suppresses compatibility.

Returning to $A_1 \neq 0$, there will be exponentially many bidiagonal states [see comments on domain walls below Eq. (2.13)], with ergodicity breaking selecting one of many textural "replicas"[34] at minima of a rugged free-energy landscape. For different initial conditions, i.e., changing the random seed σ_{random}, but other thermal-history parameters unchanged, we land in other degenerate local minima with locally different bidiagonal textures. A similar influence of initial conditions was seen earlier for single-diagonal martensitic domain walls.[9] The crossover temperatures are also weakly affected.

We now examine further a given set of textures. Within the annealing period, it is convenient to henceforth measure times from cessation of cooling, i.e., as functions of $\tilde{t}=t-t_{\text{final}}$, and to further drop the superscript, $\tilde{t}\to t=0,1,2,\ldots,t_h$. We discover that the phases, obviously *nonuniform* in space, can also be *dynamic* in time. If we take the sum/difference of textures at unit time steps,

$$\sigma_{\pm}(\vec{r},t)=\frac{1}{2}\{\sigma(\vec{r},t+1)\pm\sigma(\vec{r},t)\}, \tag{5.1}$$

color plots (not shown) of $\sigma_+(\vec{r},t)$ for both the feathery phase and the maze phase are mostly zero, so oscillating with period 2, while σ_+ for the bidiagonal phase looks like Fig. 4(b) and is thus static. The "velocity" or σ_- plots is complementary. (The possibility of oscillating/static phases is seen in a simple uniform mean-field map, $\sigma_0(t+1)\simeq -\tanh[D_0 g_0 \sigma_0(t)]$, which has solutions $\sigma_0(t)\simeq\pm(-1)^t$ for $g_0(\tau)>0$ and $\sigma_0\simeq\pm 1$ for $g_0(\tau)<0$.)

To pin down textural oscillations more precisely, we define generalizations of Eq. (5.1) using wavelet transforms as in signal processing and compression. The method has been described as more powerful than Fourier transforms in that it can simultaneously resolve signals both in time and frequency, and wavelets have been used to analyze chaotic behavior.[28] In continuous-time signal processing, the usual focus is on finer time resolutions/higher harmonics; here we consider discrete time in unit steps and larger time intervals/subharmonics. First we consider auxiliary functions, which are a sum and a difference of unit-height functions, nonzero only within the "unphysical" time intervals $1/2\geq t>0$ and $1\geq t>1/2$,

$$\psi^{\pm}_{0,0}(t)=h(t\{1-2t\})\pm h(\{2t-1\}\{2-2t\}), \tag{5.2a}$$

where $h(t)$ is the Heaviside step function. (To avoid numerical ambiguity at the jumps, it is convenient to add a positive quantity to t in the step function, e.g., $t\to t+0.25$.) We define functions that are nonzero only in time intervals $1/\nu_j\geq t>0$ where the time extent or "period" is $1/\nu_j=1/2^j=2^{|j|}=2,4,8,\ldots$, with negative integer $j=-|j|$. The inverse time extent or "frequency" is then $\nu_j=2^j=1/2,1/4,1/8,\ldots$. A set of these *finite-extent* square-normalized functions is defined as

$$\psi^{\pm}_{j,0}(t)=\sqrt{\nu_j}\,\psi^{\pm}_{0,0}(\nu_j t). \tag{5.2b}$$

Since our discrete-time step has $j\neq 0$, the set $\{\psi^{-}_{j,0}(t)\}$ excludes the $\psi^{-}_{0,0}(t)$ auxiliary function (5.2a).

With discrete-time shifts $t\to t-t_j$ where $t_j(m)\equiv m/\nu_j$ with integer $m=0,1,2,3,\ldots$ one defines

$$\psi^{\pm}_{j,m}(t)=\psi^{\pm}_{j,0}(\nu_j t-m), \tag{5.2c}$$

which is nonzero only for a time window $(m+1)/\nu_j\geq t>m/\nu_j$. The time shifts just slide the finite-extent profiles along the time axis. The functions of Eq. (5.2c) are, of course, the Haar "wavelet" (ψ^-) and "scaling" (ψ^+) functions.[28] Since $t\leq t_h=2^M$ in our case, the shifts are restricted to $t_j+1/\nu_j\leq t_h$ or $t_j/t_h\leq 1-1/(\nu_j t_h)$, so m values are in the range $m_{\max}\equiv(2^{M-|j|}-1)\geq m\geq 0$. A square wave in time $t\leq t_h$ with period $2^{|j|}$ is then just a sum over shifts of the finite-extent functions, $\Sigma_m \psi^{-}_{j,m}(t)$.

We focus on wavelets and extract simple diagnostics. The overlap of a signal $\sigma(\vec{r},t)$ with the Haar-wavelet functions is a local "wavelet transform,"[28] with a discrete-time t sum over $t_h\geq t>0$. We define

$$W^{-}(\vec{r},\nu_j,t_j)\equiv\sum_t \sigma(\vec{r},t)\psi^{-}_{j,m}(t). \tag{5.3a}$$

For $1/\nu_{j=-1}=2$ and $t_j(m=0)=0$ we essentially recover σ_- of Eq. (5.1). To capture the static part we simply consider the time average,

$$\bar{\sigma}(\vec{r})\equiv\frac{1}{t_h}\sum_t \sigma(\vec{r},t). \tag{5.3b}$$

At a given site $\vec{r}$ and after a time t_j, the overlap $W^{-}(\vec{r},\nu_j,t_j)$ is a measure of the signal subsequently having positive and negative segments of total extent $1/\nu_j$. From Eq. (5.3a), two complementary diagnostics for oscillations can be defined.

(i) To get a local-site spectrum of frequencies ν_j at a site $\vec{r}$, which appear at any time during the annealing period t_h, we take the average of Eq. (5.3a) over all allowed time shifts $t_j(m)$ (with $0\leq m\leq m_{\max}$),

$$W_1(\vec{r},\nu_j)\equiv\frac{1}{m_{\max}}\sum_m W^{-}[\vec{r},\nu_j,t_j(m)]. \tag{5.4}$$

(ii) To get a global diagnostic for a frequency ν_j after a time shift t_j, a spatial average of Eq. (5.3a) is not suitable since it just picks out the $\vec{k}=0$ mode. So we square before taking a site average: this gives a projection of an autocorrelation that will be considered later,

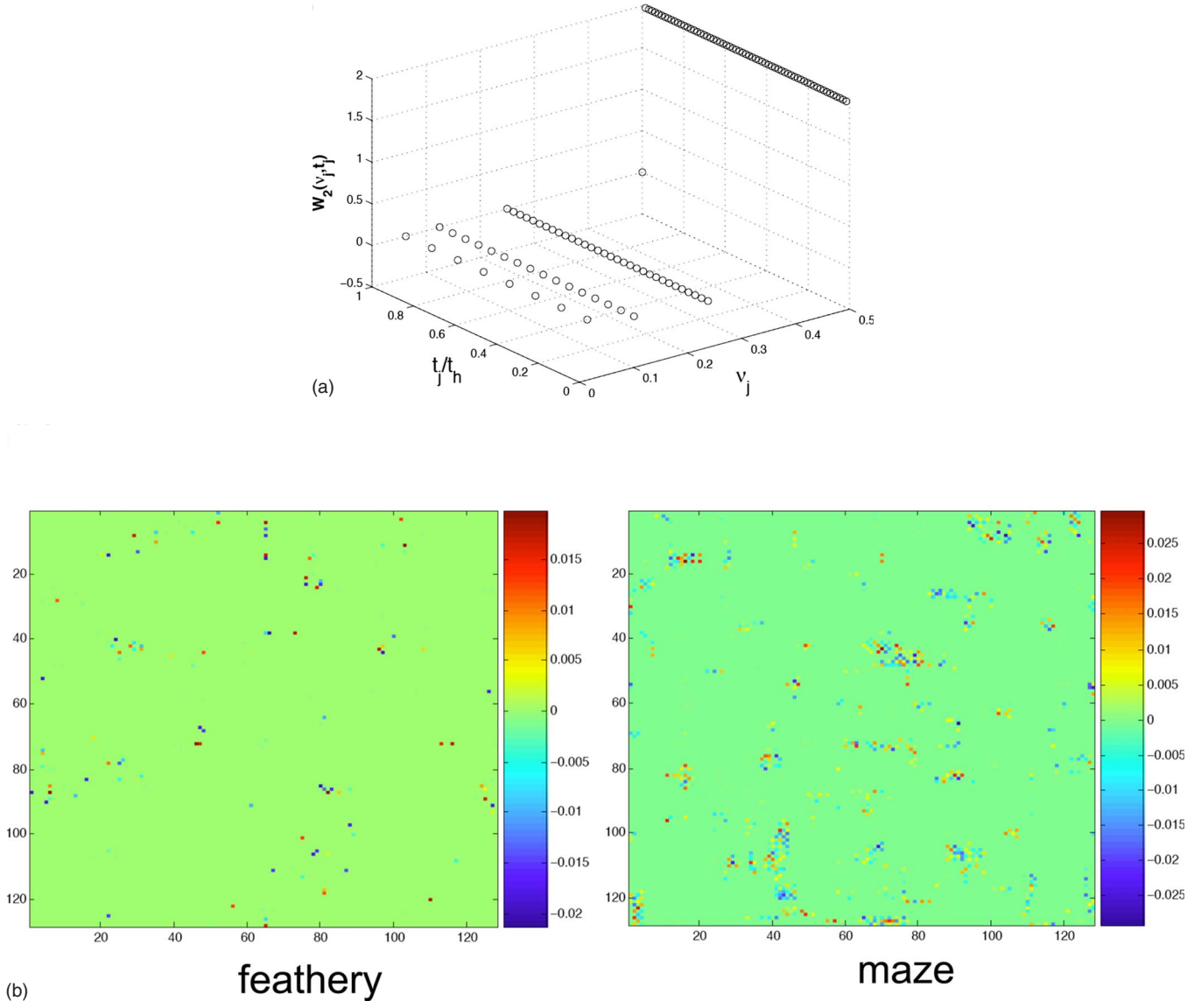

FIG. 5. (Color online) Periodicity of textures, in the three phases, seen through a Haar-wavelet analysis: (a) maze phase relief plot of lattice-averaged Haar spectrum of Eq. (5.5) or $W_2(\nu_j,t_j)$ versus frequency ν_j and time shift t_j/t_h scaled in the holding time, showing ridges at the frequencies. (b) Color plots of the local-site spectrum [Eq. (5.4)] or $W_1(\vec{r},\nu_j)$ versus (x,y) for $\nu_j=1/4$ showing minority frequency, small-amplitude oscillation clusters, within the predominantly period-two feathery and maze phases.

$$W_2(\nu_j,t_j) \equiv \frac{1}{N}\sum_{\vec{r}} \{W^-(\vec{r},\nu_j,t_j)\}^2 = \sum_{t,t'} \psi^-_{j,m}(t)\psi^-_{j,m}(t') \times \left\{ \frac{1}{N}\sum_{\vec{r}} \sigma(\vec{r},t)\sigma(\vec{r},t') \right\}. \quad (5.5)$$

A square wave $\sigma(\vec{r},t)=\sigma(\vec{r},0)(-1)^t$ would show up in a relief plot of $W_2(\nu_j,t_j)$ versus ν_j and t_j, as a ridge peaked at the frequency $\nu_j=1/2$, and constant along the time-shift axis. An average of Eq. (5.5) over m is a global frequency spectrum: $W_3(\nu_j)\equiv\Sigma_m W_2(\nu_j,t_j(m)/m_{\max}$.

Figure 5(a) shows a relief plot of $W_2(\nu_j,t_j)$ versus ν_j and t_j/t_h for the maze phase. The periodic square-wave ridge of $\nu_j=1/2$ is clearly the majority frequency, with subharmonics 1/4, 1/8 being about 10^{-2} smaller. These correlated sign flips of the narrow domain-wall stripes are reminiscent of short wavelength oscillatory "dyadon" modes of twin arrays.[6] The feathery phase has a similar W_2 and the low-temperature bidiagonal phase has $W_2=0$ (both not shown). The spectrum $W_3(\nu_j)$ thus drops to zero below τ^*, so vibrational textural contributions to the entropy vanish.

Figure 5(b) shows the local-site spectra $W_1(\vec{r},\nu_j)$ of Eq. (5.4) for a minority frequency $\nu_j=1/4$ in the feathery and maze phases. Most sites are majority frequency so W_1 is zero (background), but there are isolated minority-frequency clusters of weak amplitude square waves, which are somewhat more numerous in the maze phase. The plots with $\nu_j=1/8,1/16$ are similar. With κ synchronized clusters and $N_1,N_2,\ldots,N_\kappa$ sites in each cluster, the feathery and maze attractors are thus neither chaotic $(\kappa=N;N_1=1,\ldots,N_\kappa=1)$ nor fully coherent $(\kappa=1;N_1=N)$ but are possibly partially

ordered or dynamically glassy.[27,34] A plot of $W_1(\vec{r},\nu_j)$ for the bidiagonal phase with $\nu_j=1/2,1/4$ (not shown) is entirely zero, so there are no oscillating clusters.

How can these square-wave rapid oscillations at the nanolevel coexist with apparently static global-level thermodynamic functions of Fig. 3. Going back to the mean-field maps of Eq. (3.4), we see that a sign flip of all the $\sigma(\vec{r},t)$ local inputs flips the signs of the $\sigma(\vec{r},t+1)$ local outputs, while the free energy of Eq. (4.3c) is even in the variables. Thus, a period-two $\sigma(\vec{r},t)=\sigma(\vec{r},0)(-1)^t$ square wave would give time-independent contributions $\sim|\sigma(\vec{k},t)|^2=|\sigma(\vec{k},0)|^2$ to Eqs. (4.3a), (4.3b), and (4.3c). At τ^* there is a period-halving threshold, as these period-two oscillations convert on cooling to period-one or static attractors. This vanishing of the vibrational entropy leaving only the configurational entropy of textures, which simultaneously coarsen, helps us to understand the change in slope or elbow in the excess entropy of Fig. 3(b). For infinite holding times we expect monodiagonal twinned martensite: the bidiagonally glassy state will be a long-lived metastable fixed point. Nonlinear maps can have long-lived transients through a mechanism of "intermittency" near the instability of a limit cycle attractor.[27]

B. Dynamic transition pathways

But if the spatiotemporal textures are locally stable, then how can there be a transition from one phase to the other on cooling. These are mediated by transient "acoustic bursts," riding on these square-wave "phonons."

The three textures of Fig. 4 well within the three temperature regions are stable over long holding times. However, as τ_g and τ^* are approached in different cool-and-hold runs, the attractors show their metastability and convert *locally* to the low-temperature phase. The changes in thermodynamic functions of Fig. 3 are thus smooth rather than sharp. For example, by annealing at fixed temperature $\tau=-0.05>(\tau_g=-0.95)$, the feathery phase incubates small patches of the maze phase, part of a broad gradual transformation, completed by τ_g. Similarly, by cooling to $\tau=-1.17>(\tau^*=-1.57)$ and annealing, the maze phase converts after an incubation delay $t\sim10^2$ to finite patches of the bidiagonal phase, i.e., shows static islands in an oscillating sea. The rather gradual feathery/maze and more dramatic maze/bidiagonal conversions are shown in Figs. 6(a) and 6(b), respectively, through pictures at early and intermediate times.

Both Figs. 6(a) and 6(b) conversions show light-color spots, as seen in earlier continuous-time simulations of the continuum-variable strain[9] $e_2(\vec{r})$. These hotspots act as *configurational catalysts*. They build up in number and become correlated, and as in Fig. 6(b), it can incubate the transforming regions within a "catalytic corral" and then disappear. The mobile hotspots are dynamical heterogeneities, facilitating the opening of conversion channels to other local textures, and are reminiscent of chains of high-velocity atoms in molecular-dynamics simulations of glassy systems.[4] When the catalysts dry up for $\tau\ll\tau^*$, further relaxation pathways, e.g., from the glassy bidiagonal state to the martensitic monodiagonal state, take very long times: there is a structural arrest in a literal sense. The catalytic droplets emerge spontaneously from a kinetically unbiased dynamics, differing from models[21,22] where specific neighboring configurations are imposed, for spin-flip transitions to occur. Although there are no hard spheres here, the hotspots clearly have conceptual similarities to free-volume scenarios in glasses.[1]

We investigate hotspots further. Figure 6(c) has a blowup of a region in the conversion of Fig. 6(b), showing the long, winding, narrow stripes of the maze phase and the emerging bidiagonal coarser textures. There are lighter unit-cell squares where a martensitic two-variant interface or d_2 domain-wall splits into two martensite-austenite d_1 domain walls, which later rejoin, with the order parameter going toward zero inside the enclosed droplet [see comments below Eq. (2.7)]. The hotspots are thus like ϕ^6 dark solitons of sign opposite to their background, attached to the domain-wall line solitons.[36] For cool and hold to $\tau=-2$ and then applying a uniform external tilt $p(\vec{r})=p_0$ in Eq. (2.10a), the map [Eq. (3.3b)] changes as $Q(\vec{r})\to Q(\vec{r})-(D_0/2\epsilon)p_0$. For a large enough $p_0=3\epsilon$ say, the bidiagonal state converts to a $\sigma_0=1$ uniform state, again through the mediation of hotspots along the domain walls.

The compressional $e_1(\vec{r},t)$ and shear $e_3(\vec{r},t)$ strains can be evaluated from expressions $e_i(\vec{k})/\epsilon=B_{i,2}\sigma(\vec{k},t)$ above Eq. (2.5a). The maze phase $e_2\sim\sigma$ oscillating stripes show up also as stripes in e_1,e_3 but with less patterning in e_3. The bidiagonal disordered phase has trapped compressional and shear strains, unlike the sharp monodiagonal twins that expel non-OP strains.[9] The transient hotspots with deviatoric dips are also in regions of low compressional and shear strains, so are austenitic droplets of the high-temperature square-unit-cell phase.

Since $1-S(\vec{r})^2$ is nonzero (and unity) only at $S(\vec{r})=0$ sites, we use a related mean-field diagnostic $\eta(\vec{r},t)\equiv([\sigma(\vec{r},t)^2]-\sigma(\vec{r},t)^2)^2$ for hotspots, shown in Fig. 6(d), comparing well with Fig. 6(c). The spatial average $\eta(t)\equiv[\eta(\vec{r},t)]$ is a global measure of the hotspot density. Figure 7(a) for $\eta(t)$ versus time t (after cooling has ceased) shows an initially fluctuating rise and delayed peaking or incubation and a sharp falloff, followed by a flattening to zero. The inset shows η for a separate cool-to-zero sweep versus the temperatures τ swept through, with two peaks that are close to τ^* and τ_g. The nonmonotonic behavior shows that hotspots are dynamically generated and temperature varying and are not just a fraction of a high-temperature phase passively swept along by a cooling ramp.[37] Hotspot wavelet analyses will be done elsewhere.

The finite lifetime of the hotspots of Fig. 6(b), after cool and hold to $\tau=-1.17$ just above τ^*, is defined as where $\eta(t)$ first flattens to zero. Figure 7(b) shows that an extrapolated plot of the austenitic hotspot lifetime versus τ vanishes linearly in $\tau-\tau_K$. The curve shows a nonlinear rise in the lifetime further away from τ_K, and the peak in $\eta(t)$ is also tracked. Thus, $\tau_K<\tau^*$ is the lower bound for appreciable hotspot generation by coupled-map lattice and so is a "dynamic lower spinodal temperature" for the catalysts.

Kauzmann[2] conjectured that T_K was a metastability limit of a supercooled liquid phase, with a profusion of freely nucleated polycrystallites, then forming a "glass," as also found in a plaquette-spin model.[2,15] Our interpretation is complementary: the catalytic droplets are active lubricants

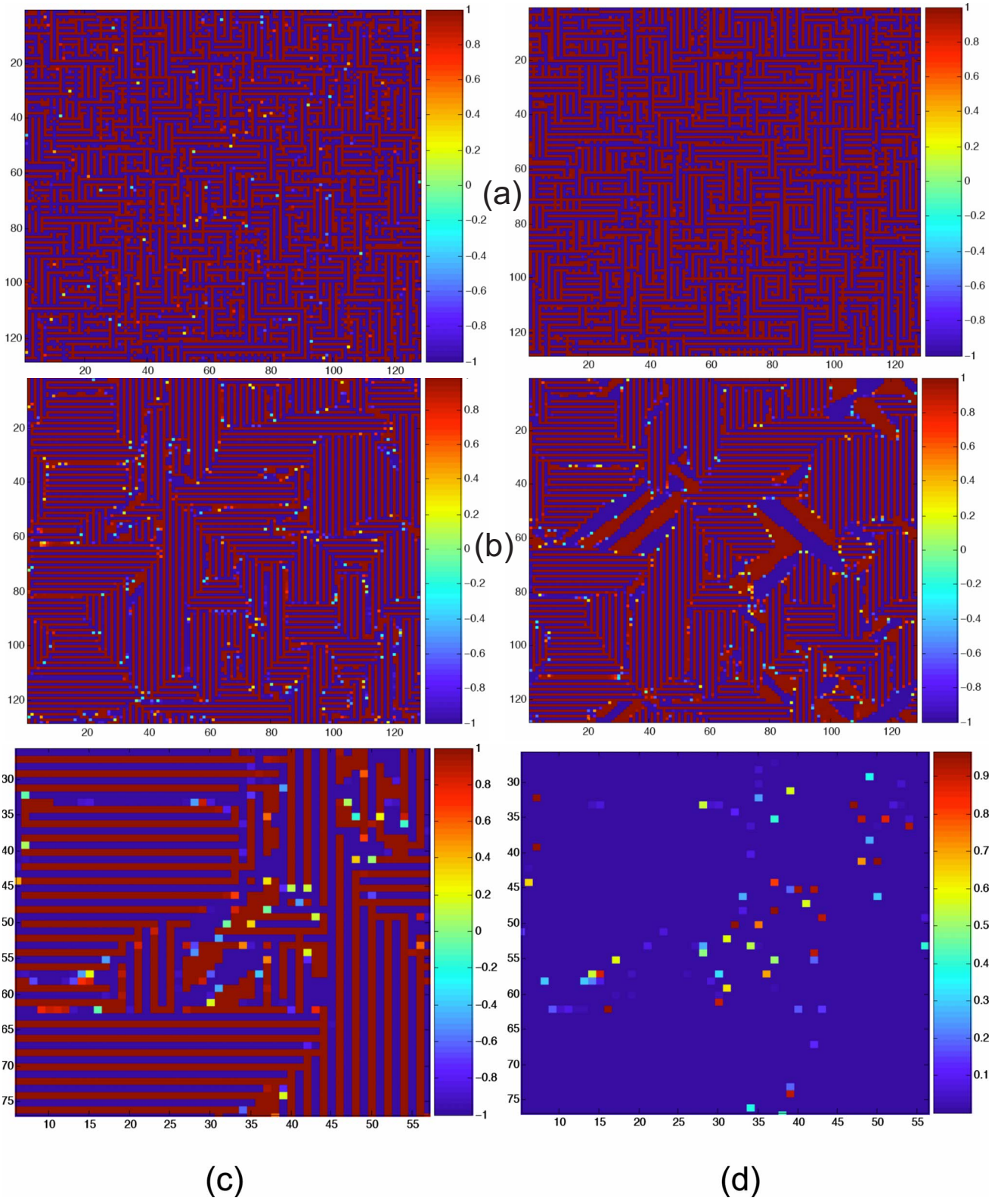

FIG. 6. (Color online) Role of the correlated dynamics of hotspots in local textural conversions after cool and hold at $|\dot{T}|=0.001$ to fixed holding temperatures just above the crossovers $\tau_g=-0.95$ and $\tau^*=-1.57$: (a) local conversion with time of the feathery to the maze phase at fixed $(\tau=-0.05)>\tau_g$. The light spots are low-strain austenitic hotspots that bracket the emerging maze patch and then disappear. (b) Local conversion with time of the maze to the bidiagonal phase at fixed $(\tau=-1.17)>\tau^*$. The hotspots form transient catalytic corrals. (c) Blowup of the $\sigma(\vec{r},t)$ maze/bidiagonal conversion region of (b), showing lighter austenitic droplets attached to martensitic domain walls. (d) Blowup of local hotspot diagnostic $\eta(\vec{r},t)$ in the same maze/bidiagonal conversion region compare with (c).

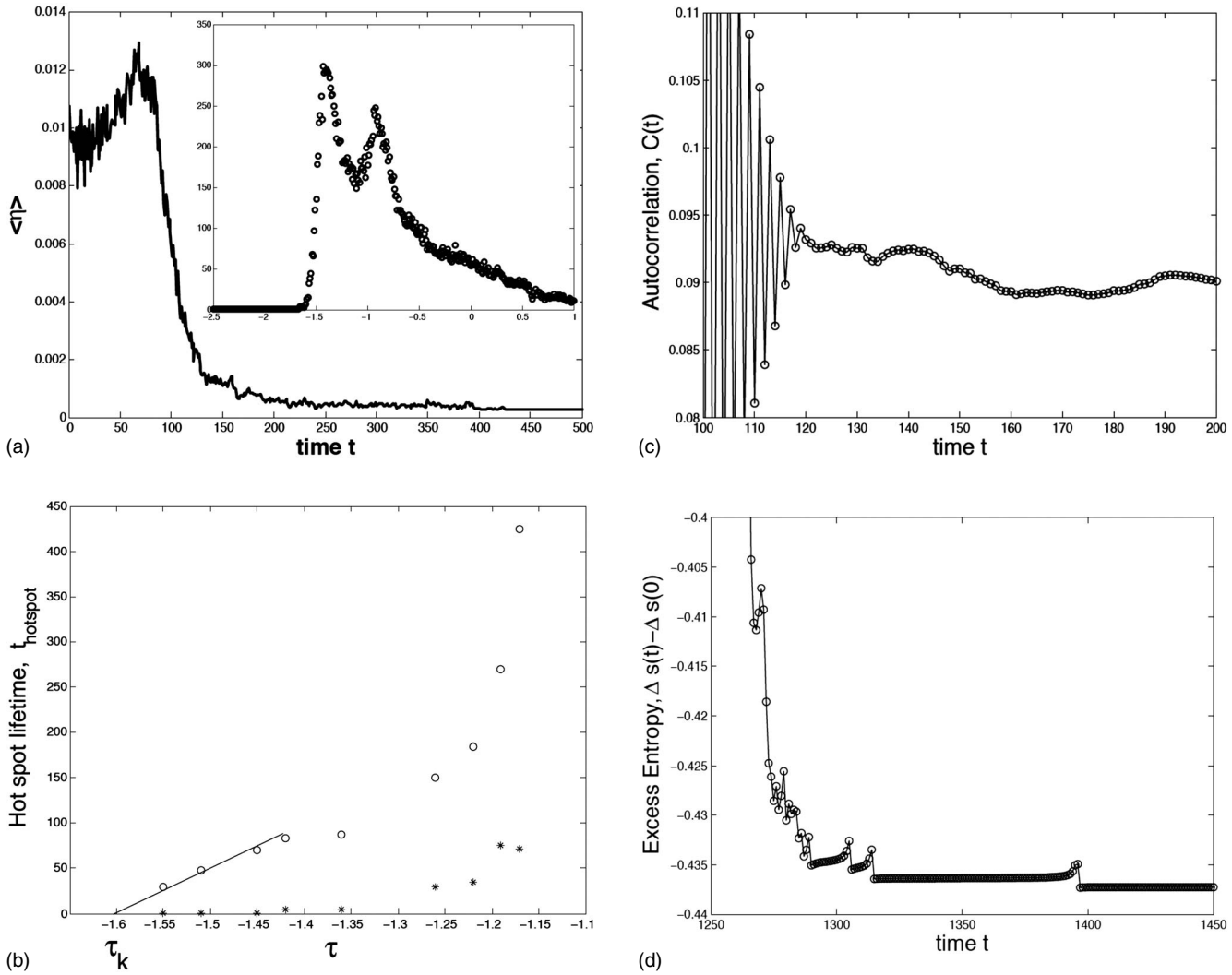

FIG. 7. Global hotspot diagnostic, pseudospin autocorrelations, and entropy relaxation at the maze/bidiagonal conversion of Fig. 6(b) for $|\dot{T}|=0.001$ with cool and hold to $\tau=\tau_{\text{final}}=-1.17$: (a) global hotspot diagnostic $\eta(t)$ versus t, with time measured after cooling ceases. [Inset: η versus temperatures τ swept through during a separate cooling run to $\tau_{\text{final}}=-9$.] (b) Plot of hotspot lifetime versus holding temperature τ for cooling rates $|\dot{T}|=0.001$ (open circles); the hotspot peaking time is also tracked (asterisks). (c) Pseudospin autocorrelation of Eq. (5.6) or $C(t)$ versus t. (d) Excess entropy $\Delta s(t)-\Delta s(0)$ versus t.

rather than passive competitors. Glassy freezing occurs not at a supercooling limit T_c for pre-existing austenite but at a $T_K<T_c$ dynamic-generation limit, where the austenitic droplets have zero survival time. The vanishing of catalysts at τ_K should induce a slowing[2] of textural conversions; this will be studied elsewhere. It would be interesting if catalytic droplets of the high-temperature phase, e.g., paramagnetic zero-spin clusters, could be identified in other spin models,[14,15] without imposed kinetic constraints.[21,22]

C. Correlations and dampings

We define a pseudospin autocorrelation function averaged over all sites,

$$C(t)=\sum_{\vec{r}}\sigma(\vec{r},t)\sigma(\vec{r},0)/\sum_{\vec{r}}\sigma^2(\vec{r},0), \tag{5.6}$$

related to the curly brackets of Eq. (5.5). Figure 7(c) shows $C(t)$ versus time after cooling ceases for the maze/bidiagonal conversion of Fig. 6(b) at $\tau=-1.17>\tau^*$, showing damped oscillations. In glasses, correlations show two types of damping, not yet fully understood.[1] Comparing $C(t)$ of Fig. 7(c) and $\eta(t)$ of Fig. 7(a), one sees that there is a link between the time variations. At early times, when $C(t)$ starts with large-amplitude rapid spin oscillations, the $\eta(t)$ hotspot density is appreciable and thus induces a relatively strong (β) damping by catalyzing formation of the static competing phase. At later times, when the residual $C(t)$ has small-amplitude slow spin oscillations, the density $\eta(t)$ is small, and there is a weaker (α) damping from now-sparser hotspots. The different evolution regimes of the hotspot density thus induce different damping regimes in the pseudospin correlation.

The configurational relaxation, monitored through $\Delta s(t)-\Delta s(0)$ in Fig. 7(d), shows that the entropy is released unusually in decreasing steps bracketed by rise/dip spikes, as entropy barriers are crossed. With a local applied stress, the same behavior occurs, with slightly higher entropy steps.

VI. DISCUSSION

We have considered a strain pseudospin Hamiltonian with compatibility-induced power-law anisotropic couplings, reduced from a martensitic-transition free energy. The order-parameter equation for local mean fields is solved iteratively under constant-rate cooling between initial and final temperatures, followed by annealing for a long holding time at the final temperature. We obtain spatiotemporal textures and thermodynamics of this coupled-map lattice under cooling. The entropy excess (over the uniform-state Landau value) shows a weak roll-off at $T=T_g$ and a sharper elbow at a lower $T=T^*$ above a Kauzmann-type temperature T_K.[2] The thermodynamic crossover temperatures correspond to changes in domain-wall diagnostics and decrease logarithmically with cooling rate. The macroscopic "static" thermodynamics conceals a rich nanoscopic spatiotemporal dynamics. There are at least three long-lived textural attractors of inherent-structure domain walls that emerge on cooling, namely, a feathery phase of labyrinthine domain walls, and a gradual local conversion completed by T_g to a maze phase of irregular tiles of narrow domain-wall stripes in horizontal/vertical directions. Both these textural phases temporally switch sign with period 2, with minority-frequency subharmonic clusters. Finally at T^* there is freezing to a static low-temperature phase of coarser domain-wall patterns along both diagonals. The suppression of vibrational states explains the excess-entropy elbow at T^*. There are many textural realizations of a given phase, accessed by changing the random initial state. Deep inside temperature regimes, the phases are stable over long times. However, as crossover temperatures T_g, T^* are approached, conversions between phases occur locally by waiting at fixed temperature for an incubation time to elapse. Transitions between textures are facilitated by austenitic hotspots correlated in space and time, which catalyze local regions of the new incubated phase and then disappear. The lifetime of incubated hotspots vanishes at T_K, identified with a dynamic spinodal temperature for generating the austenitic catalysts. Different pseudospin-damping regimes are induced by different catalyst-density regimes.

Our model has a PLA-coupled, but kinetically unbiased, iterated-map dynamics (with temperature-controlled parameters), high-degeneracy metastable states (e.g., of bidiagonally oriented domain walls), and hotspot catalysts (that are internally generated, not imposed). It differs from other models where degenerate excited states and kinetically biased transitions are specified by the model assumptions. A key result is that large-scale textural conversions on cooling can be catalytically induced by a low density of dynamical hotspots, which are like momentarily dipping saddle points of an evolving free-energy surface. When they become rare, entropy barriers rise, and in an ergodicity-breaking transition, the system is left trapped in one of the many minima of a now-rigid and rugged free-energy landscape.[1]

We now make some speculative comments about the relevance of these ideas for further possible work. Experimentally, acoustic emission has been seen associated with martensitic transitions;[38] it would therefore be interesting to relate this, and any athermal square-wave signals, through a wavelet analysis to hotspots or periodic attractors. Martensitic transitions have broad transformation regions, as does the model. Complex oxides, with strain coupled to spin and charge, can show multiscale patterns and glassy behavior, including long martensitic "incubation" times on change in control parameters, slow oscillation of mesoscopic textures, or glassy aging phenomena.[10,39] These might be related to an iterative delay in dynamically building up hotspot correlations to mediate the transition, to long-period attractors, or to entropy barriers. Varying material parameters $A_1, \xi, T_0 - T_c$ and adding quenched compositional disorder, one could try to model strain glasses with suppressed martensitic transitions.[11] More generally, one might explore "metastable materials," whose functionality depends on the understanding and control of their glassy multivariable texturing. Such materials would have extended phase diagrams with preparation parameters $|\dot{T}|$ and $1/t_h$ as added variables, where the equilibrium phase diagram is a slice at the origin of the added axes.

Quite apart from its martensitic motivation, Hamiltonians (2.10a) and (2.10b) with anisotropic interactions could be studied as a statistical model analytically and in Monte Carlo simulations[32] under a temperature ramp or a temperature sawtooth for hysteresis. Other extensions of the Blume-Capel model to include isotropic Ruderman-Kittel-Kasuya-Yosida (RKKY) interactions or slower power laws have been considered.[19,40]

Unusual thermodynamic behaviors including multiple spinodal branches, disturbance propagation, and multivalley free energies have been found in models with isotropic long-range interactions.[18,19,41] For the glass transition, mode-coupling approaches exist.[1] One could similarly analyze our model with PLA interactions of zero spatial average, which are a border case of long-range interactions.

Simulations of coupled-map lattices have studied oscillation/synchronization of clusters.[27,34,35] One might consider, for this PLA-coupled model, a stability analysis of period-altering thresholds on cooling, temperature-dependent Liapunov exponents, and mechanisms for long-lived metastable attractors.[19,27,34]

For configurational glasses,[1] the model suggests a speculative scenario of "glass as a metastable fixed point of a map" based on analogs. Suppose, with cooling rate faster than the emptying rate of the liquid well,[37] we can avoid crystallization and supercool to one of the many nonuniform-density metastable branches. Taking the uniform austenite and twinned martensite phases as analogous to the equilibrium liquid and crystal phases, the feathery/maze phases are like the supercooled liquid with vibrationally hidden structure,[3] and the coarser static bidiagonal phase is like the frozen "ideal glass" or amorphous state.

Strain variables have been found useful in describing amorphous or glassy phases.[42] One might consider a dynamic or coupled-map lattice version of the glassy density-functional treatment of Dasgupta,[5] which allows for a range of possible grid scales and orientations. To treat emerging and transient textures of distorted unit cells, one could include gradients of the density $\rho(\vec{r})$ or harmonic-strain contributions on the family of grids [e.g., $E_{\mu\nu}(\vec{r})^2 \sim [\Delta_\mu \Delta_\nu \rho(\vec{r})]^2$] added to the density-density structure-factor interactions. A

no-topological-defect constraint on the unstirred slowly cooled melt would then induce strain-strain PLA potentials. The (scalar) density and (tensor) strain variables would be analogous to two-OP glass scenarios.[43] The inherent structures[3] would be patterns of solid-solid (d_2) domain walls between two or more competing variants in vibrating heterogeneous icebergs, which could include icosohedral structures. The liquid states would have a competitive/catalytic dual role: squeezed out externally as textured icebergs expand but generated internally as transient catalysts, with d_2 walls thermally splitting/rejoining into two d_1 walls enclosing droplets. Correlated chains[4] of these transient droplets could dynamically mediate the rearrangement, growth, and merger of the textured regions. If they have time to complete their work, one gets a single-variant crystal. If cooled below a T_g, the evolution could become facilitator limited, with $T^* \sim T_K$ reached before rearrangements are completed. The catalysts disappear, the fixed-point metastable attractor dominates, and the remaining coarser tangle of trapped d_2 walls is left high and dry, frozen into a glassy/amorphous structure. The temperature-dependent increase in the activation energy on cooling (that defines a fragile glass) could be related to the vanishing lifetime at $T=T_K$ of the liquid hotspots. At very low temperatures, in a mechanism independent of material details, the trapped d_2 walls could split due to quantum fluctuations, into higher-energy d_1 droplets and rejoin, with ranges of local trapped-stress values providing ranges of two-level splittings.[1,44]

The pseudospin model is thus motivated by martensitic transitions and leads to a coupled-map lattice with power-law anisotropic interactions that shows behavior analogous to configurational glasses. The model can be useful for further studies relevant to these three fields.

ACKNOWLEDGMENTS

It is a pleasure to thank H. Cerdeira, K. P. N. Murthy, V. S. S. Sastry, and S. Sinha for useful conversations. We are grateful to NSERC and ICTP, Trieste for partial support.

[1] K. Binder and W. Kob, *Glassy Materials and Disordered Solids* (World Scientific, Singapore, 2005); Z. Nishiyama, *Martensitic Transformations* (Academic, New York, 1978).
[2] W. Kauzmann, Chem. Rev. (Washington, D.C.) **43**, 219 (1948).
[3] F. H. Stillinger and T. A. Weber, Phys. Rev. A **25**, 978 (1982); S. Sastry, P. G. Debenedetti, and F. H. Stillinger, Nature (London) **393**, 554 (1998).
[4] C. Donati, J. F. Douglas, W. Kob, S. J. Plimpton, P. H. Poole, and S. C. Glotzer, Phys. Rev. Lett. **80**, 2338 (1998).
[5] C. Dasgupta, Europhys. Lett. **20**, 131 (1992); Pramana **64**, 679 (2005).
[6] G. R. Barsch, B. Horovitz, and J. A. Krumhansl, Phys. Rev. Lett. **59**, 1251 (1987); B. Horovitz, G. R. Barsch, and J. A. Krumhansl, Phys. Rev. B **43**, 1021 (1991).
[7] M. Baus and R. Lovett, Phys. Rev. Lett. **65**, 1781 (1990); Phys. Rev. A **44**, 1211 (1991).
[8] S. Kartha, T. Castán, J. A. Krumhansl, and J. P. Sethna, Phys. Rev. Lett. **67**, 3630 (1991); S. Kartha, J. A. Krumhansl, J. P. Sethna, and L. K. Wickham, Phys. Rev. B **52**, 803 (1995).
[9] S. R. Shenoy, T. Lookman, A. Saxena, and A. R. Bishop, Phys. Rev. B **60**, R12537 (1999); K. O. Rasmussen, T. Lookman, A. Saxena, A. R. Bishop, R. C. Albers, and S. R. Shenoy, Phys. Rev. Lett. **87**, 055704 (2001); T. Lookman, S. R. Shenoy, K. O. Rasmussen, A. Saxena, and A. R. Bishop, Phys. Rev. B **67**, 024114 (2003); D. M. Hatch, T. Lookman, A. Saxena, and S. R. Shenoy, *ibid.* **68**, 104105 (2003).
[10] S. R. Shenoy, T. Lookman, and A. Saxena, in *Magnetism and Structure in Functional Materials*, Springer Series in Materials Science, edited by A. Planes, L. Manosa, and A. Saxena (Springer, New York, 2005).
[11] Y. Wang, X. Ren, and K. Otsuka, Phys. Rev. Lett. **97**, 225703 (2006).
[12] H. Shintani and H. Tanaka, Nat. Phys. **2**, 200 (2006); P. Harrowell, *ibid.* **2**, 157 (2006).
[13] S. Prosandeev and L. Bellaiche, Phys. Rev. B **75**, 094102 (2007).
[14] J. D. Shore, M. Holzer, and J. P. Sethna, Phys. Rev. B **46**, 11376 (1992).
[15] A. Cavagna, I. Giardina, and T. S. Grigera, Europhys. Lett. **61**, 74 (2003); P. Dimopoulos, D. Espriu, E. Jane', and A. Prats, Phys. Rev. E **66**, 056112 (2002).
[16] P. Bak, Phys. Rev. Lett. **46**, 791 (1981).
[17] J. Bechhoefer, H. Löwen, and L. S. Tuckerman, Phys. Rev. Lett. **67**, 1266 (1991).
[18] J. Schmalian and P. G. Wolynes, Phys. Rev. Lett. **85**, 836 (2000).
[19] *Dynamics and Thermodynamics of Systems with Long-Range Interactions*, Lecture Notes in Physics Vol. 602, edited by T. Dauxois, S. Ruffo, E. Arimondo, and M. Wilkens (Springer, New York, 2002); A. Rapisarda and A. Pluchino, Europhys. News **36**, 202 (2005).
[20] E. Bayong, H. T. Diep, and V. Dotsenko, Phys. Rev. Lett. **83**, 14 (1999).
[21] F. Ritort, Phys. Rev. Lett. **75**, 1190 (1995); M. L. Mansfield, Phys. Rev. E **66**, 016101 (2002).
[22] J. P. Garrahan and D. Chandler, Phys. Rev. Lett. **89**, 035704 (2002); M. Sellitto, J. Phys.: Condens. Matter **14**, 1455 (2002).
[23] D. Elderfield and D. Sherrington, J. Phys. C **16**, L1169 (1983); A. Erzan and E. Lage, *ibid.* **16**, L555 (1983).
[24] M. Tarzia and M. A. Moore, Phys. Rev. E **75**, 031502 (2007).
[25] T. Lookman, S. R. Shenoy, and A. Saxena, Bull. Am. Phys. Soc. **49**(1), 1315 (2004).
[26] M. Blume, Phys. Rev. **141**, 517 (1966); H. W. Capel, Physica (Amsterdam) **32**, 966 (1966); M. Blume, V. J. Emery, and R. B. Griffiths, Phys. Rev. A **4**, 1071 (1971).
[27] J. Crutchfield and K. Kaneko, in *Directions in Chaos*, edited by Hao Bai-Lin (World Scientific, Singapore, 1987), Vol. 2; K. Kaneko, Physica D **41**, 137 (1990).
[28] C. S. Burns, R. A. Gopinath, and H. Guo, *Introduction to Wavelets and Wavelet Transforms* (Prentice-Hall, Englewood Cliffs, NJ, 1998); C. Chandre, S. Wiggins, and T. Uzer, Physica D **181**,

171 (2003).

[29] We note that (a) the strains $E_{\mu\nu}=e_{\mu\nu}+g_{\mu\nu}$ that enter the free energy actually depend on, $e_{\mu\nu}$, the symmetric part of the distortion tensor plus a "geometric nonlinearity" part, $g_{\mu\nu}$, quadratic in the symmetrized distortion and in local rotations. We work in the limit that the geometric nonlinearity is negligible, so the linearized strain is the symmetrized distortion. We can thus loosely refer to a "strain representation," although strictly speaking, it is a "distortion representation." The compatibility constraint actually applies to the distortion tensor (Ref. 30). (b) The definitions in Eqs. (2.1) and (2.4b) of $e_3=2E_{xy}$ and $O_3=K_xK_y$ have factors of 2 and 1/2 compared to earlier work (Refs. 9 and 10). The compatibility condition has the product O_3e_3 and so is unchanged.

[30] S. R. Shenoy, T. Lookman, and A. Saxena (unpublished).

[31] E. Vives, J. Goicoechea, J. Ortin, and A. Planes, Phys. Rev. E **52**, R5 (1995); P. A. Lindgard and O. G. Mouritsen, Phys. Rev. Lett. **57**, 2458 (1986).

[32] N. Shankaraiah, K. P. N. Murthy, S. R. Shenoy, and T. Lookman (unpublished).

[33] Variational distributions diagonal in coordinate space (Ref. 26) are clearly inappropriate in our spatially nonlocal PLA model. A purely uniform mean field would yield a slightly different self-consistency equation.

[34] S. C. Manrubia and A. S. Mikhailov, Europhys. Lett. **50**, 580 (2000); **53**, 451 (2001); M. G. Cosenza and A. Parravano, Phys. Rev. E **64**, 036224 (2001).

[35] S. Sinha, Phys. Rev. E **66**, 016209 (2002).

[36] S. N. Behera and A. Khare, Pramana **15**, 245 (1980); F. Falk, Z. Phys. B: Condens. Matter **51**, 177 (1983); U. Roy, R. Atre, C. Sudheesh, C. N. Kumar, and P. K. Panigrahi, arXiv:0708.3646 (unpublished).

[37] S. R. Shenoy and G. S. Agarwal, Phys. Rev. A **29**, 1315 (1984); K. P. N. Murthy and S. R. Shenoy, *ibid.* **36**, 5087 (1987).

[38] E. Vives, J. Ortín, L. Mañosa, I. Ràfols, R. Pérez-Magrané, and A. Planes, Phys. Rev. Lett. **72**, 1694 (1994).

[39] V. Hardy, A. Maignan, S. Hébert, C. Yaicle, C. Martin, M. Hervieu, M. R. Lees, G. Rowlands, D. Mc K. Paul, and B. Raveau, Phys. Rev. B **68**, 220402 (2003); W. Wu, C. Israel, N. Hur, S. Park, S.-W. Cheong, and A. de Lozanne, Nature Mater. **5**, 881 (2006); P. Chaddah, K. Kumar, and A. Banerjee, Phys. Rev. B **77**, 100402(R) (2008).

[40] T. Balcerzak and J. W. Tucker, J. Magn. Magn. Mater. **278**, 87 (2004).

[41] A. Torcini and S. Lepri, Phys. Rev. E **55**, R3805 (1997).

[42] S. Alexander, Phys. Rep. **296**, 65 (1998).

[43] H. Tanaka, J. Chem. Phys. **111**, 3163 (1999).

[44] P. W. Anderson, B. Halperin, and C. M. Varma, Philos. Mag. **25**, 1 (1972); W. A. Phillips, J. Low Temp. Phys. **7**, 351 (1972).